

Chapter 2

Ultrafast Electron Crystallography: Principles and Dynamics[†]

[†]Part of this chapter was adapted from D.-S. Yang, N. Gedik, A. H. Zewail, *J. Phys. Chem. C* **111**, 4889 (2007).

Introduction

The geometric nature in the structure analysis of a molecule or a crystal by electron diffraction shares a high degree of similarity with that by x-ray diffraction. The geometrical theory originally developed for x-ray crystallography can, therefore, be used in electron crystallography, and its relevance to our technique is described in this chapter. The major dissimilarities between these two diffraction methods originate from the different radiation–matter interactions. Because x-ray is an electromagnetic wave, its scattering—Thomson scattering if the energy is conserved—is caused by the (polarizable) electron density in the electron shells of the atoms; atomic nuclei are very poorly affected by the electromagnetic field and, hence, invisible to such radiation. Consequently, structure analysis of x-ray diffraction deals with the distribution of electron density that is often concentrated around the nuclei. For electron interaction with matter, however, it is the Coulomb force that governs the scattering because electrons are charged particles, and as a result, the electrostatic potential due to both the positively charged atomic nuclei and their electron clouds should be considered. On the basis of the different interactions involved, the average magnitude of the atomic scattering amplitude of electrons is about 10^3 times that of x-ray, leading to a ratio of 10^6 for the scattered intensities (I). Therefore, electrons are strongly scattered by matter, which grants electron diffraction with a higher sensitivity for the probing of nanometer-scale and interfacial structures and in the detection of small structural changes in time.

Before the presentation of the geometrical theory, a quick summary for quantitative description of the intensities of the scattered beams is given here. Derivation of the kinematic (elastic) scattering theory for electron diffraction starts from the time-dependent Schrödinger equation and considers a propagating plane wave for the

incident electrons (I-3),

$$\Psi_0(\vec{r}', t) = A \exp[i(\vec{k}_i \cdot \vec{r}' - \omega t)] \quad (1)$$

where A denotes the amplitude, \vec{k}_i the incidence wavevector, and ω the angular frequency. The relativistic effect needs to be taken into account for highly accelerated electrons,

$$eV_0 = \sqrt{(m_0^2 c_0^4 + p^2 c_0^2)} - m_0 c_0^2 \quad (2)$$

where V_0 is the acceleration voltage (in volt), m_0 the electron's rest mass, p the electron's momentum, and c_0 is the speed of light. According to the de Broglie relation, the electron's wavelength (λ) is equal to h/p and, therefore, can be expressed (in Å) by (4)

$$\lambda = h / \sqrt{2m_0 e V_0 (1 + e V_0 / 2m_0 c_0^2)} = 12.26 / \sqrt{V_0 (1 + 0.9785 \times 10^{-6} V_0)}. \quad (3)$$

With the use of the mathematical tool of Green's function, the scattered wave derived in the asymptotic limit for large- L , far-field detection (i.e., Fraunhofer diffraction that is typically the case for crystallographic measurements) and under the first Born approximation is given by (I-3)

$$\Psi_s(\vec{L}) = -\frac{A e^{i\vec{k}_i \cdot \vec{L}}}{4\pi L} \int U(\vec{r}) \exp[i(\vec{k}_i - \vec{k}) \cdot \vec{r}] d^3 \vec{r}, \quad (4)$$

where \vec{k} is the outgoing wavevector ($|\vec{k}| = |\vec{k}_i|$) along the direction of \vec{L} , $U(\vec{r}) = (2m e / \hbar^2) V(\vec{r})$ is the reduced potential associated with the electrostatic potential of the scattering object, $V(\vec{r})$, and the integration runs over the occupied volume.

Therefore, the kinematic theory of electron scattering (Eq. 4) can be deduced with the use of the theory of Fourier integrals, defining the relative scattering amplitude

$$f(\vec{s}) \equiv \frac{1}{4\pi} \int U(\vec{r}) \exp(-i\vec{s} \cdot \vec{r}) d^3 \vec{r} \quad (5)$$

with the momentum transfer vector

$$\vec{s} \equiv \vec{k} - \vec{k}_i. \quad (6)$$

The observed diffraction intensities, $I(\vec{L}) = |\Psi_s(\vec{L})|^2$, are therefore in proportion to $|f(\vec{s})|^2$ (1, 2). The detailed structure in the potential of the specimen (thereby the spatial arrangement of atoms) is given by

$$U(\vec{r}) = \frac{1}{8\pi^3} \int 4\pi f(\vec{s}) \exp(i\vec{s} \cdot \vec{r}) d^3\vec{s}. \quad (7)$$

Thus, these results provide the theoretical basis for the geometrical theory considering the periodic lattice structure in real space and its Fourier transform, the periodic reciprocal lattice, in reciprocal (k) space.

If $U(\vec{r})$ is substituted by a sum of reduced atomic potentials, $U_j^a(\vec{r} - \vec{r}_j)$ (displaced according to their central positions in a crystal), where j refers to the j th atom,

$$U(\vec{r}) = \sum_j U_j^a(\vec{r} - \vec{r}_j), \quad (8)$$

Equation 5 can be rewritten as

$$f(\vec{s}) = \frac{1}{4\pi} \sum_j \exp(-i\vec{s} \cdot \vec{r}_j) \int U_j^a(\vec{r} - \vec{r}_j) \exp[-i\vec{s} \cdot (\vec{r} - \vec{r}_j)] d^3\vec{r} = \sum_j f_j(\vec{s}) \exp(-i\vec{s} \cdot \vec{r}_j) \quad (9)$$

with the definition of the atomic scattering factor, $f_j(\vec{s})$, being

$$f_j(\vec{s}) \equiv \frac{1}{4\pi} \int U_j^a(\vec{r}) \exp(-i\vec{s} \cdot \vec{r}) d^3\vec{r}. \quad (10)$$

The assumption here is that $U_j^a(\vec{r})$ in a crystal is approximately the same as that for an isolated atom (i.e., the valence electrons affect the electron scattering to a very minor extent). Although the absolute values of diffraction intensities may show small deviation from the kinematic theory described above, it will become clear that, from the various studies successfully made, the kinematic approximation is capable of capturing the most important information from the observed diffraction changes in time and, therefore, suitable for the structural dynamics studies using electron diffraction.

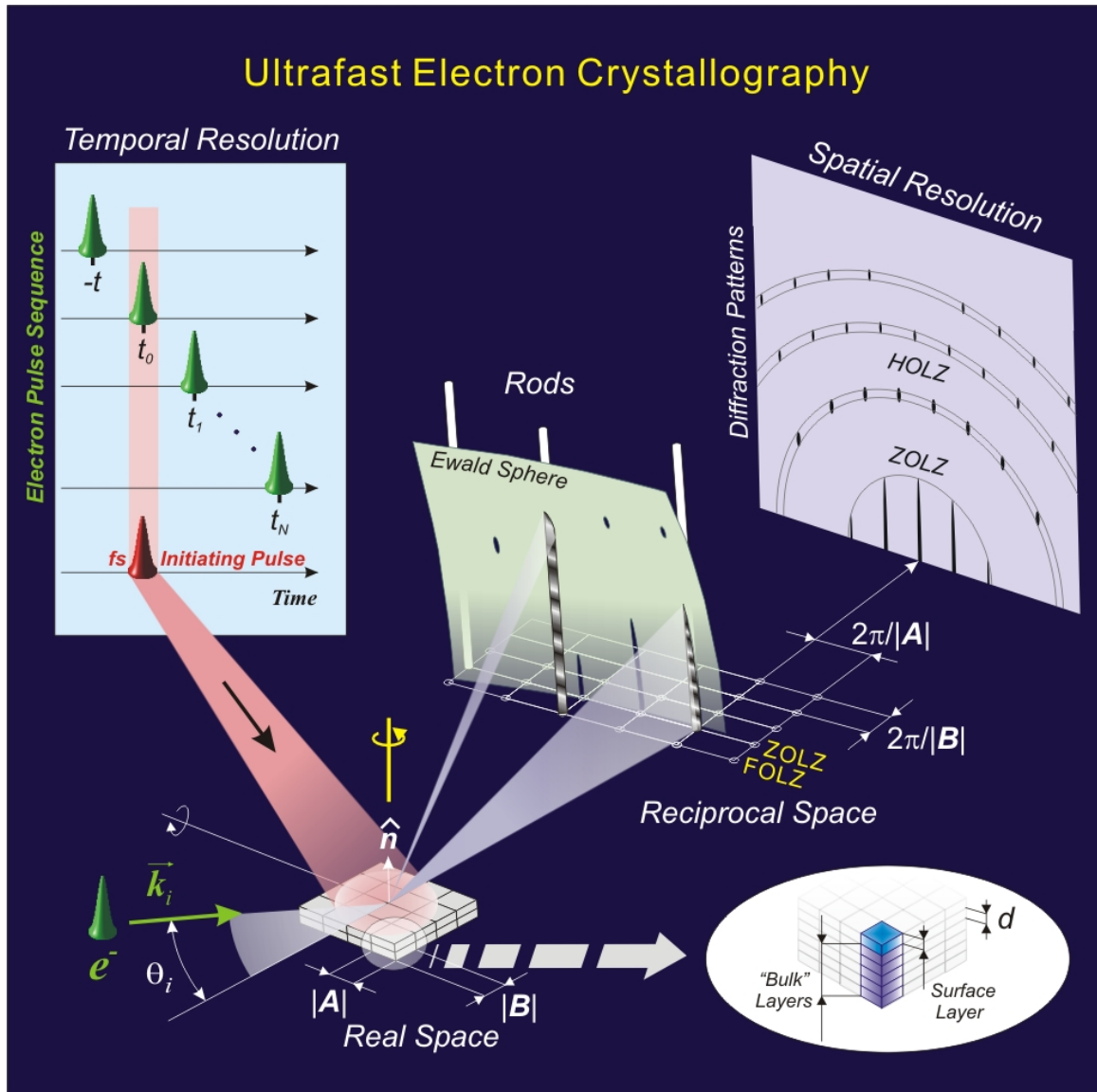


Fig. 1. Schematic of the methodology of UEC in the reflection geometry. The relationship between real and reciprocal lattices and Ewald construction for the formation of diffraction patterns are shown (see Text and Figs. 2 to 4 for details). The temporal and spatial resolutions of UEC are achieved by varying the delay time between the electron probe and initiating heating pulses (upper left), and the recording of the diffraction patterns at different times.

From the discussion below, it is straightforward to see that the geometrical theory for high-energy electron diffraction is much simpler than that for x-ray diffraction because of the very short electron wavelength used. Ultrafast electron crystallography (UEC), a time-resolved electron diffraction technique for condensed-matter studies, can be performed in two modes, reflection or transmission geometry. The implementation in the reflection geometry (Fig. 1) enables us to determine time-resolved nonequilibrium structures of a crystal surface region or adsorbate near the interface, and also their equilibrium structures at steady state. The transmission geometry allows the detection of structures and dynamics of nanometer-scale specimens. In what follows, the theoretical foundation to determine structures, their inhomogeneity, and the corresponding temporal evolution is examined. A typical diffraction image may show a pattern of Bragg spots, streaks, Debye–Scherrer rings, Kikuchi lines or bands, or a combination of these with a scattering background. By monitoring and comparing the changes of different diffraction features, such as position, intensity, width, and shape, we can obtain a more complete picture of structural dynamics. Experimental test cases (gold and silicon) are also provided in this chapter to illustrate the principles invoked.

A. Equilibrium Structures

A.1. Diffraction in Reflection

Spots or rings in an electron diffraction pattern are the result of the constructive interference of scattered waves from different lattice points. In UEC, the electrons have large kinetic energy ($eV_0 = 30$ keV) and therefore a small de Broglie wavelength, $\lambda \sim 0.07$ Å from Eq. 3, which is a few percent of a typical atomic spacing (the reason behind the resolution of interatomic distances through diffraction). For elastic scattering, the criterion of constructive interference is described by the Bragg condition:

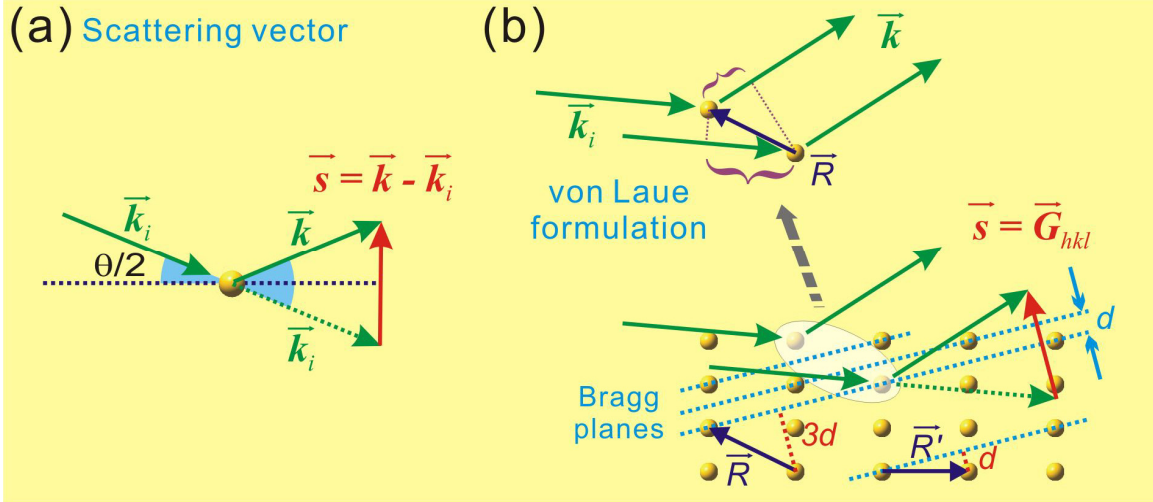


Fig. 2. (a) Vectorial representation for the elastic scattering process. The incidence angle $\theta_1 = \theta/2$ and the scattering vector \vec{s} are shown. (b) Upper: The von Laue condition of constructive interference. The phase difference between two outgoing waves scattered by two atoms separated by \vec{R} is indicated by the curly brackets. Lower: Comparison of the von Laue and Bragg formulations for constructive interference conditions. Note that \vec{s} is parallel to the interplanar distance d under investigation (i.e., perpendicular to the Bragg planes under probing), and any vector of the real lattice has a projection onto the \vec{s} direction to be an integer multiple of d .

$$n\lambda = 2d \sin(\theta/2), \quad (11)$$

which is simply the result of considering crystal planes of reflections; n is the order of diffraction, d is the distance between adjacent parallel crystal planes, and θ is the total angle of deflection from the initial beam. Because λ is known, in principle, if n is known, the measurement of θ gives d . In practice, the interplanar distance d can be obtained from rocking curves by changing the incidence angle and recording spots of two consecutive orders, n and $n + 1$, thus removing the need for assigning the absolute precise magnitudes of n and θ (see below).

The equivalent picture given by the von Laue formulation considers the geometrical phase shifts of the scatterers themselves. For elastic scattering, because the wavevectors of the incident and scattered electrons (\vec{k}_i and \vec{k}) have the same amplitude ($|\vec{k}| = |\vec{k}_i| = 2\pi/\lambda$), the scattering vector (Eq. 6) yields $s = |\vec{s}| = (4\pi/\lambda)\sin(\theta/2)$; see Fig. 2a for the vectorial representation and Appendix A for the convention used. The phase matching of the scattered waves from all scatterers is required for constructive interference (Eq. 9), which means that for all vectors \vec{R} connecting atoms of the Bravais lattice in real space, the Laue condition is satisfied when $\exp(i\vec{s} \cdot \vec{R}) = 1$, or equivalently, when $\vec{s} \cdot \vec{R} = 2m\pi$ where m is an integer (Fig. 2b, upper). It is noted that the same equation leads to the Bragg condition by substituting the amplitude of \vec{s} and recognizing that the projection of \vec{R} along the \vec{s} direction equals to m times the interplanar distance d (Fig. 2b, lower). Therefore, the Bragg planes under probing are perpendicular to \vec{s} , and

$$s d = 2n\pi \quad (12)$$

where n is the order of diffraction. Experimentally, since the appearance of a Bragg spot indicates the direction of \vec{k} , with the knowledge of \vec{k}_i , the crystal planes involved can be deduced since they are always perpendicular to \vec{s} (Fig. 2b, lower).

Incidentally, the reciprocal lattice, which is the Fourier transform of the real lattice spanned by three basis vectors (\vec{a} , \vec{b} and \vec{c}), can be constructed by three reciprocal basis vectors, \vec{a}^* , \vec{b}^* and \vec{c}^* , which satisfy the following relationship of inner product:

$$\begin{aligned} \vec{a} \cdot \vec{a}^* = \vec{b} \cdot \vec{b}^* = \vec{c} \cdot \vec{c}^* = 2\pi \quad \text{and} \\ \vec{a} \cdot \vec{b}^* = \vec{b} \cdot \vec{c}^* = \vec{c} \cdot \vec{a}^* = \vec{b} \cdot \vec{a}^* = \vec{c} \cdot \vec{b}^* = \vec{a} \cdot \vec{c}^* = 0. \end{aligned} \quad (13)$$

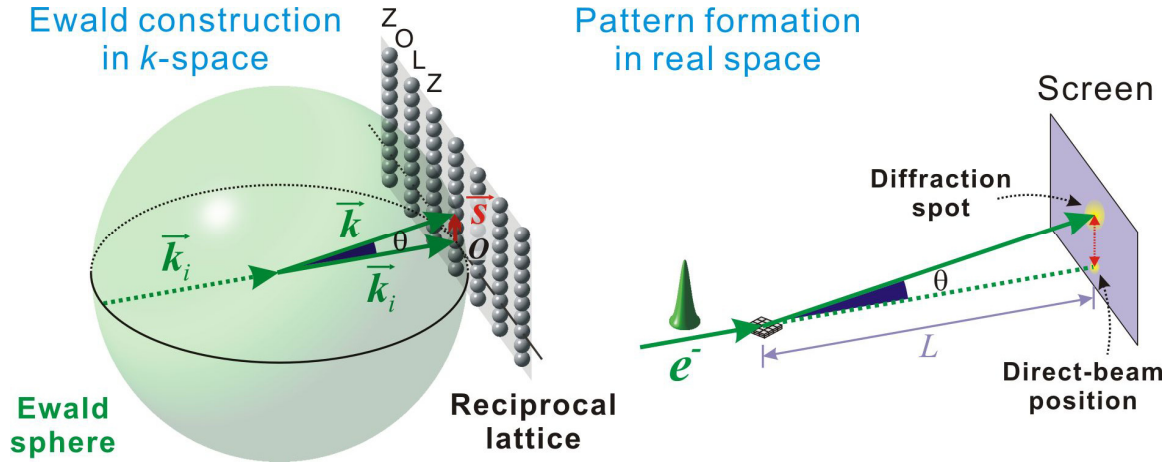


Fig. 3. Left: Ewald construction in k space. The Ewald sphere passes through the origin O of the reciprocal lattice, and any other intersections between the sphere and reciprocal points (rods) give diffraction spots or streaks. Right: Diffraction pattern formation.

The mathematical formulas for \vec{a}^* , \vec{b}^* and \vec{c}^* are written as

$$\vec{a}^* = 2\pi \frac{\vec{b} \times \vec{c}}{\vec{a} \cdot (\vec{b} \times \vec{c})}, \quad \vec{b}^* = 2\pi \frac{\vec{c} \times \vec{a}}{\vec{b} \cdot (\vec{c} \times \vec{a})}, \quad \text{and} \quad \vec{c}^* = 2\pi \frac{\vec{a} \times \vec{b}}{\vec{c} \cdot (\vec{a} \times \vec{b})}. \quad (14)$$

Any vector (\vec{G}) in the reciprocal lattice can be expressed as their linear sum,

$$\vec{G}_{hkl} = h\vec{a}^* + k\vec{b}^* + l\vec{c}^*, \quad (15)$$

with h , k and l being integer numbers called Miller indices. Consequently, $\exp(i\vec{G} \cdot \vec{R}) = 1$ for all such vectors according to Eq. 13. The Laue condition of constructive interference is hence satisfied if and only if \vec{s} is a unique one of them, i.e., $\vec{s} = \vec{G}_{hkl}$ for certain h , k and l (Fig. 2b).

Therefore, analysis of diffraction patterns is greatly facilitated by using the reciprocal lattice and Ewald construction (5), which is based on conservation of energy and momentum of electrons. The Ewald sphere in k space is constructed such that the vector from the center of the sphere to the origin of the reciprocal space is \vec{k}_i (Fig. 3, left); the size of the Ewald sphere is entirely determined by $|\vec{k}_i|$. According to the Laue

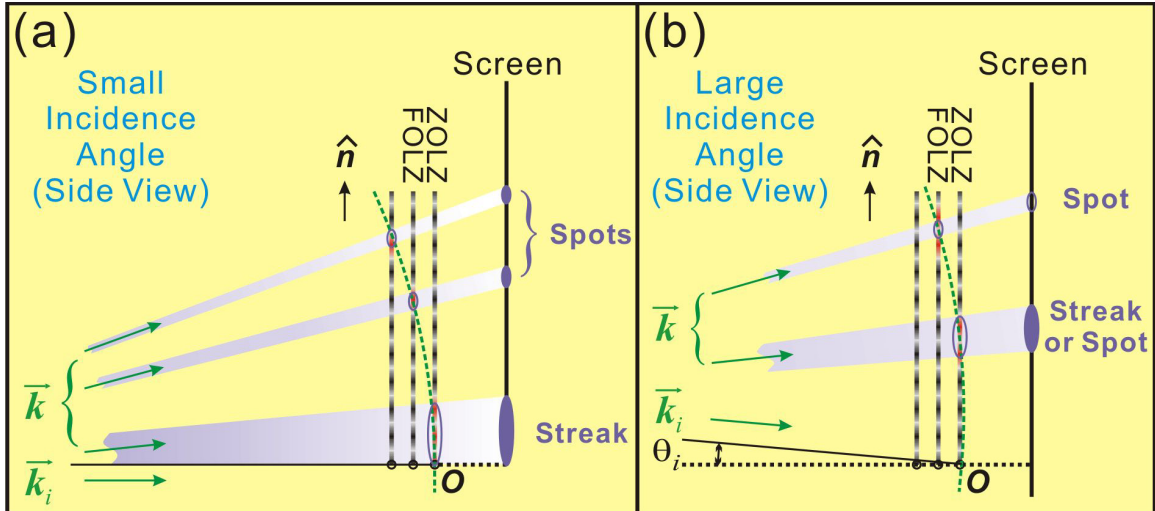


Fig. 4. (a) A side view of Ewald construction at a grazing incidence angle. The intersections between the sphere and ZOLZ (represented as a modulated reciprocal rod here) tend to form streaks, and more spots may appear at higher positions due to the sphere's intersections with HOLZ (FOLZ refers to the first-order Laue zone). (b) A side view of Ewald construction at a larger incidence angle. Diffraction streaks and/or spots will be seen at higher positions on the screen.

condition and conservation of energy and momentum for elastic scattering ($\vec{s} = \vec{k} - \vec{k}_i = \vec{G}_{hkl}$ and $|\vec{k}| = |\vec{k}_i|$), diffraction can occur when both the origin O and the reciprocal lattice point (hkl) are on the Ewald sphere (Fig. 3, left); in real space, the diffraction can be observed at that geometrical configuration (Fig. 3, right). Thus, Ewald construction provides a geometrical tool for the visualization of satisfaction of the Bragg/Laue condition.

As a note for the reciprocal lattice, reduction of the effective crystal size in real space along the surface normal direction (\hat{n}) causes the elongation of the reciprocal lattice points into “rods” along the same direction in reciprocal space, as dictated by Fourier transformation. In other words, as the third dimension of the crystal increases, the

rods change to “spots” because they become modulated by the inverse of that spacing (see Fig. 1, middle and lower right). The horizontal width of spots or rods is a measure of the degree of coherence (constructive interference) in the two dimensions of real space. The coherent diffraction is pronounced only when the reciprocal lattice intersects with the sphere (Fig. 1, middle, and Fig. 3, left).

Figure 4 provides a side view of this construction at two different incidence angles. At a grazing incidence, the diffraction pattern may consist of streaks originating from the zeroth-order Laue zone (ZOLZ, a plane in k space both passing through the origin and being perpendicular to \vec{k}_i); at higher incidence, many other spots will appear due to higher-order Laue zones (HOLZ, any other k -space planes parallel to ZOLZ but not passing through the origin) (6). The appearance of streaks or spots relies on the modulation of the reciprocal rods along the surface normal \hat{n} (a manifestation of the finite depth probed by electrons) and may also be influenced by the surface potential. However, if a zone axis of the surface is aligned perpendicular to \vec{k}_i , the horizontal spacings between streaks or spots in a diffraction pattern will correctly provide surface structural information, as shown below.

At this point, it is worth noting that the grazing incidence of electrons ($\theta_1 \equiv \theta/2$ in Fig. 2a) at an angle that is only few degrees is the required condition of reflection high-energy electron diffraction (RHEED). The reason can be easily seen from the order-of-magnitude difference between λ and typical d (on the order of an angstrom) and through Eq. 11. Similarly, by inversion, the radius of the Ewald sphere ($2\pi/\lambda$) is found orders of magnitude larger than typical reciprocal vectors (on the order of an inverse angstrom). Its major consequence is that the Ewald sphere may be approximated by a plane in the geometrical theory at the small-angle scattering condition.

So far, we only considered a perfect crystal lattice with atoms at rest (classical, $T=0$) and a perfect electron source for generating electrons with the same \vec{k}_i . The temperature effect on diffraction (loss of interference by the incoherent movements of atoms) results in loss of intensity, which is described by the Debye–Waller (DW) factors $W(T)$ (7, 8),

$$\ln \frac{I}{I_0} \equiv -2W(T) = -\frac{s^2 \langle u^2 \rangle}{3}, \quad (16)$$

where I (I_0) denotes the diffraction intensity from a lattice with (without) thermal vibrations and $\langle u^2 \rangle$ is the mean-square harmonic displacement of the constituent atoms in a unit cell. A fundamental assumption here is the thermal equilibrium among all modes of the lattice at a given well-defined temperature. However, this assumption, as shown later, is not valid when the time scale is ultrashort and/or coherent motions of atoms are involved. In regard to the electron source in reality, the small distribution of momentum of probing electrons ($\hbar \vec{k}_i$) results in broadening of Bragg spots because such an uncertainty introduces both angular wobbling of the alignment around the average \vec{k}_i and an additional thickness to the Ewald sphere.

A.2. Experimental Test Cases: Gold and Silicon

In the following discussion, we present experimental test cases [Au(111) and Si(111) surfaces] to demonstrate the extraction of structural information in our UEC studies. The existence of the specimen surface and the geometry of RHEED differentiate the 3 dimensions in space into a two-dimensional (2D) plane parallel to the surface and an axis perpendicular to it (i.e., parallel to the \hat{n}). Structural information in the former dimensions can be analyzed through azimuthal (ϕ) rotation of the specimen; the information related to the latter direction can be obtained by changing the incidence angle

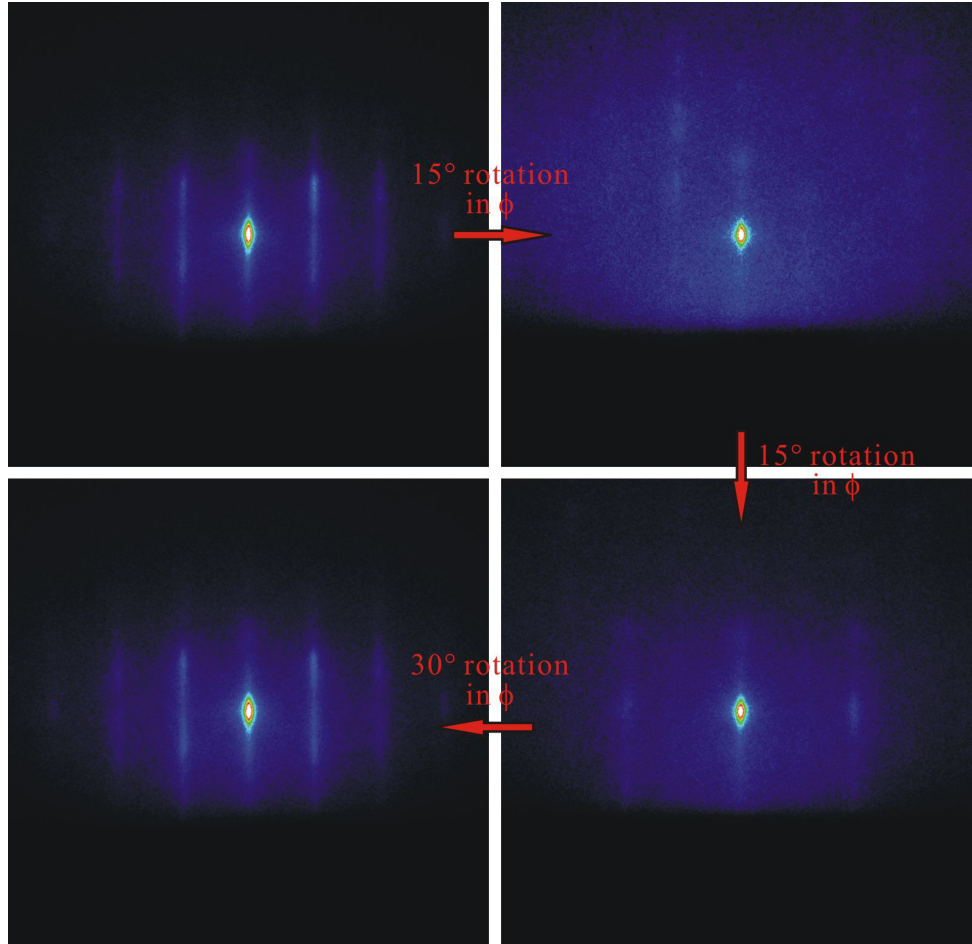


Fig. 5. Diffraction patterns (in false color) of Au(111) recorded at different azimuthal angles (ϕ). Two symmetric patterns with different horizontal spacings are obtained by 30° rotation (upper left and lower right). The same symmetric pattern is seen after a rotation of 60° in total (upper left and lower left).

(θ) of electrons, or equivalently, tilting the specimen with respect to the electron beam. We shall illustrate the principles involved with the use of the test cases.

Through azimuthal (ϕ) rotation of the Au(111) specimen, a symmetric diffraction pattern can be observed (Fig. 5, upper left) and its evolution with ϕ is shown in Fig. 5. It can be found that the same pattern appears every 60° azimuthal rotation, which signifies a 6-fold symmetry for the arrangement of the reciprocal lattice (rods) in the 2D plane

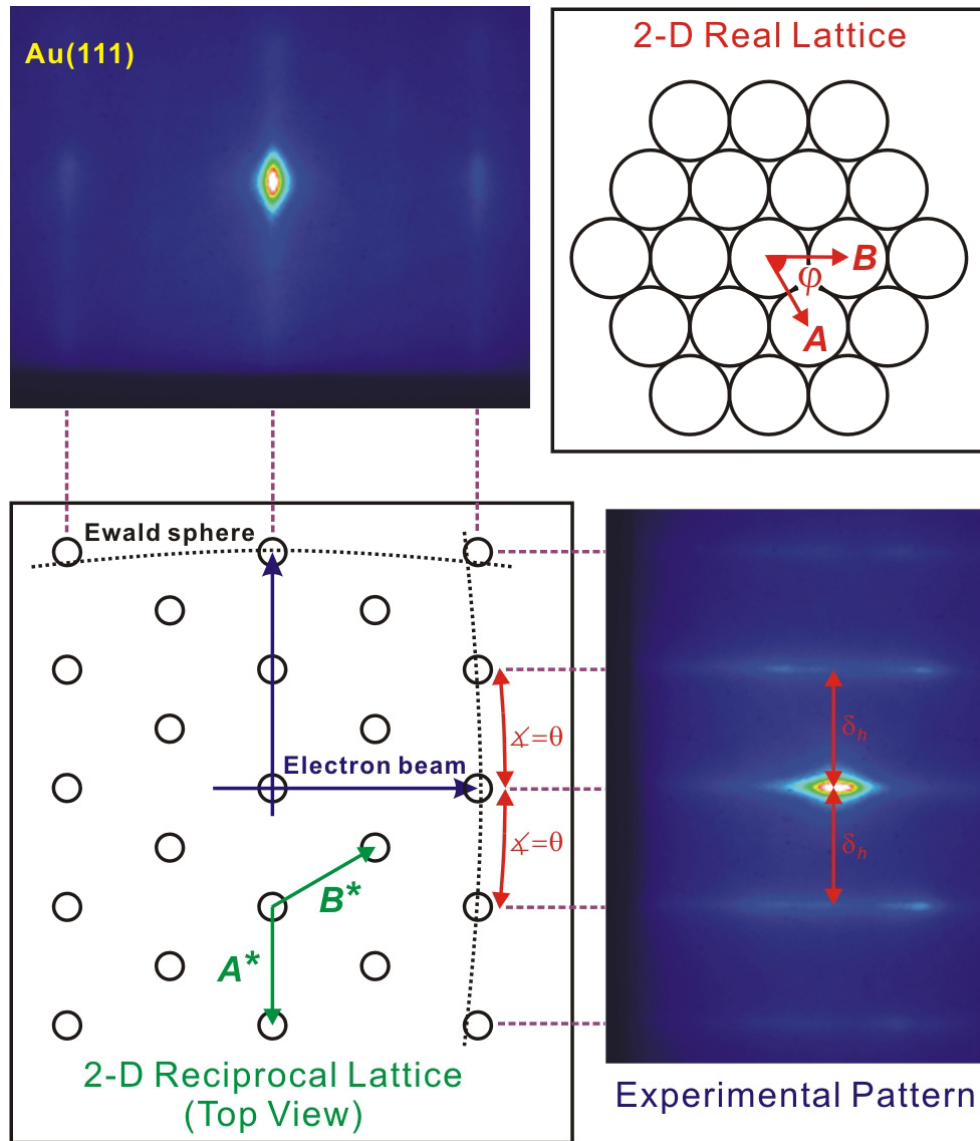


Fig. 6. Experimental and theoretical test case: Au(111) surface. Upper right: A hexagonal 2D lattice. Lower left: The top view of the corresponding reciprocal-lattice rods. The angular relationships between A , A^* and B , B^* are shown. Symmetric diffraction patterns are formed if the electrons probe the 2D lattice along the zone axes, and two examples are given here. The Ewald sphere intersects with the rods and streaks are formed on the CCD camera; the upper left and lower right panels are the experimental patterns from Au(111) at two azimuthal angles separated by 30° . The minimum spacing between diffraction streaks (δ_n) can be used to derive the 2D structural information.

parallel to the specimen surface. In fact, there are 5 different Bravais lattices in 2D (real space and reciprocal space) and for each, the characteristic ϕ is different; diffraction patterns repeat their appearance every 60° for hexagonal, 90° for square, 180° for rectangular and centered rectangular, and 360° for oblique lattices. Further verification for a certain 2D lattice can be obtained by examining the azimuthal separation between different symmetric patterns (see below). In the case of Au(111), another symmetric pattern can be observed by 30° rotation (Fig. 5, lower right).

Geometrically, two vectors, \mathbf{A} and \mathbf{B} perpendicular to the \hat{n} , form the basis of the 2D lattice in real space [see Fig. 6, upper right panel for Au(111)]. The corresponding reciprocal lattice, given by Fourier transformation, is an array of rods extended along \hat{n} with two basis vectors defined by

$$\mathbf{A}^* = 2\pi (\mathbf{B} \times \hat{n}) / |\mathbf{A} \times \mathbf{B}| \quad \text{and} \quad \mathbf{B}^* = 2\pi (\hat{n} \times \mathbf{A}) / |\mathbf{A} \times \mathbf{B}|. \quad (17)$$

Thus, $|\mathbf{A}^*| = 2\pi / |\mathbf{A}| \sin \varphi$ and $|\mathbf{B}^*| = 2\pi / |\mathbf{B}| \sin \varphi$, (18)

where φ is the angle between \mathbf{A} and \mathbf{B} (see also Fig. 1, middle). Because of these direct relationships between \mathbf{A} and \mathbf{A}^* (\mathbf{B} and \mathbf{B}^*), the azimuthal rotation in real space allow us to probe different zone axes of the reciprocal lattice for the observation of symmetric diffraction patterns (Fig. 6, lower left).

For the case of the electron beam propagating along a direction for which the ZOLZ is parallel to \mathbf{A}^* , the minimum horizontal s will be equal to $|\mathbf{A}^*|$ (Laue condition) according to Ewald construction. Therefore, the total angle of deflection

$$\theta = \tan^{-1}(\delta_h / L) = 2 \sin^{-1}(s\lambda / 4\pi) = 2 \sin^{-1}(\lambda / 2|\mathbf{A}| \sin \varphi),$$

$$L = \delta_h / \tan[2 \sin^{-1}(\lambda / 2|\mathbf{A}| \sin \varphi)], \quad (19)$$

where δ_h is the horizontal spacing between spots (rods) and L is the camera length from the scattering position to the camera. By the azimuthal rotation, which yields other

symmetric diffraction patterns, the value of φ that depends on the surface crystal structure can be determined. If L is determined independently, the lattice constants $|\mathbf{A}|$ and $|\mathbf{B}|$ can be obtained with the use of Eq. 19, and the 2D structure is thus determined.

For Au(111), the diffraction patterns taken at two zone axes (Fig. 6, upper left and lower right) correspond well with a hexagonal reciprocal lattice in 2D (Fig. 6, lower left). Therefore, the 2D structure in real space is also a hexagonal lattice with $|\mathbf{A}| = |\mathbf{B}|$. The smallest horizontal spacing between rods $[(\delta_h)_{\min}]$ recorded with $L = 17.0$ cm (Fig. 6, lower right) was 106 pixels (1 pixel = 44.94 μm in our system), which gave the experimental value of $|\mathbf{A}|$ to be 2.88(5) \AA , totally consistent with the literature x-ray value. Through 30° rotation, another zone axis was probed, and the measured spacing between adjacent rods increased and became 1.73 times $(\delta_h)_{\min}$ (Fig. 6, upper left), which was expected ($\sqrt{3}$ fold) according to the 2D structure.

Conversely, the camera length L can be accurately determined using a crystal lattice whose structure is known, and such an *in situ* measurement is free of any errors due to, e.g., rotation of the crystal. A typical error in L is $\sim 0.2\%$, which mostly originates from the spatial width and jitter of the electron pulses. However, for a given experimental setting during the time-dependent measurements, it is not the absolute values but the relative changes that are most crucial for deciphering the structural dynamics involved, and the accuracy in the determination of transient changes can be much higher (see, e.g., Chs. 4 and 5).

The third dimension, besides the surface two, of the lattice can be accessed by measurements of the rocking curve that is the change of diffraction spots with the angle of incidence, θ_i ($\equiv \theta/2$). This can be easily understood from the Bragg's formulation for the diffraction condition. For example, the diffraction patterns of Au(111) and Si(111)

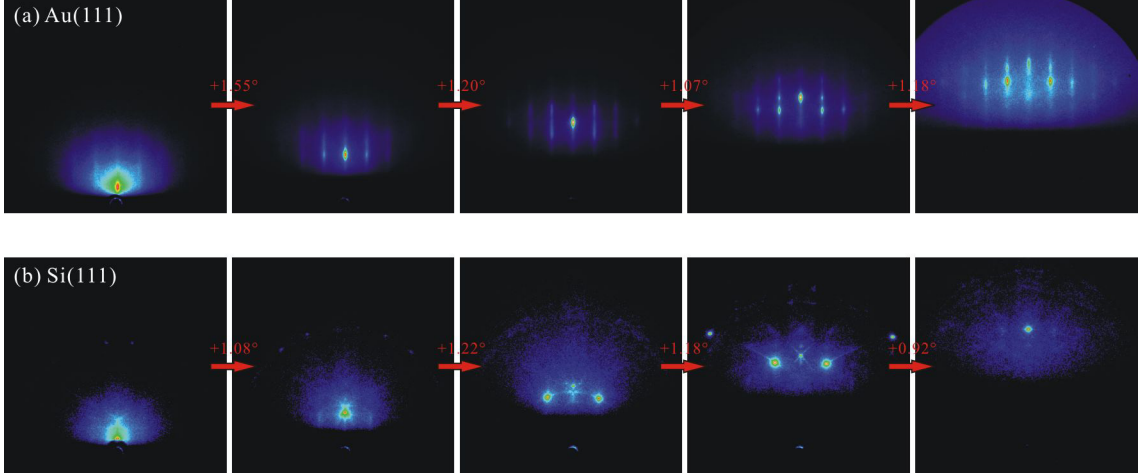


Fig. 7. Diffraction patterns (in false color) of (a) Au(111) and (b) Si(111) recorded at different incidence angles (θ_i). Gold shows rod-like diffraction patterns because it has a large atomic number and electrons can only penetrate top few layers. For silicon, other features such as Kikuchi lines and bands may interfere with rocking-curve construction.

recorded at selected incidence angles are shown in Fig. 7. By determining the angle at which successive orders appear (especially for large n , where there is less interference from 2D, other features and the refraction effect), we can obtain the vertical interplanar distance, the spacing normal to the surface. From Bragg's equation (Eq. 11), the measured change in θ_i for two consecutive orders is given, for small θ_i , by

$$\Delta\theta_i \equiv \Delta(\theta/2) \sim \sin(\theta_i + \Delta\theta_i) - \sin\theta_i = \lambda / 2d. \quad (20)$$

For consistency, d can also be obtained from the vertical separation between two consecutive spots δ_v ($\equiv \Delta s$) and with the use of the value of L , since

$$\delta_v \approx L [\tan(\theta/2 + \Delta\theta) - \tan(\theta/2)] \sim L \Delta\theta = 2L \Delta(\theta/2) \sim L\lambda / d. \quad (21)$$

Low-order Bragg spots are not used because they are affected by the refraction effect (see below), by the surface potential, morphology and quality, and of course by the presence of adsorbates. Construction of the rocking curves for the (111) surface of gold and also

Rocking-curve Construction

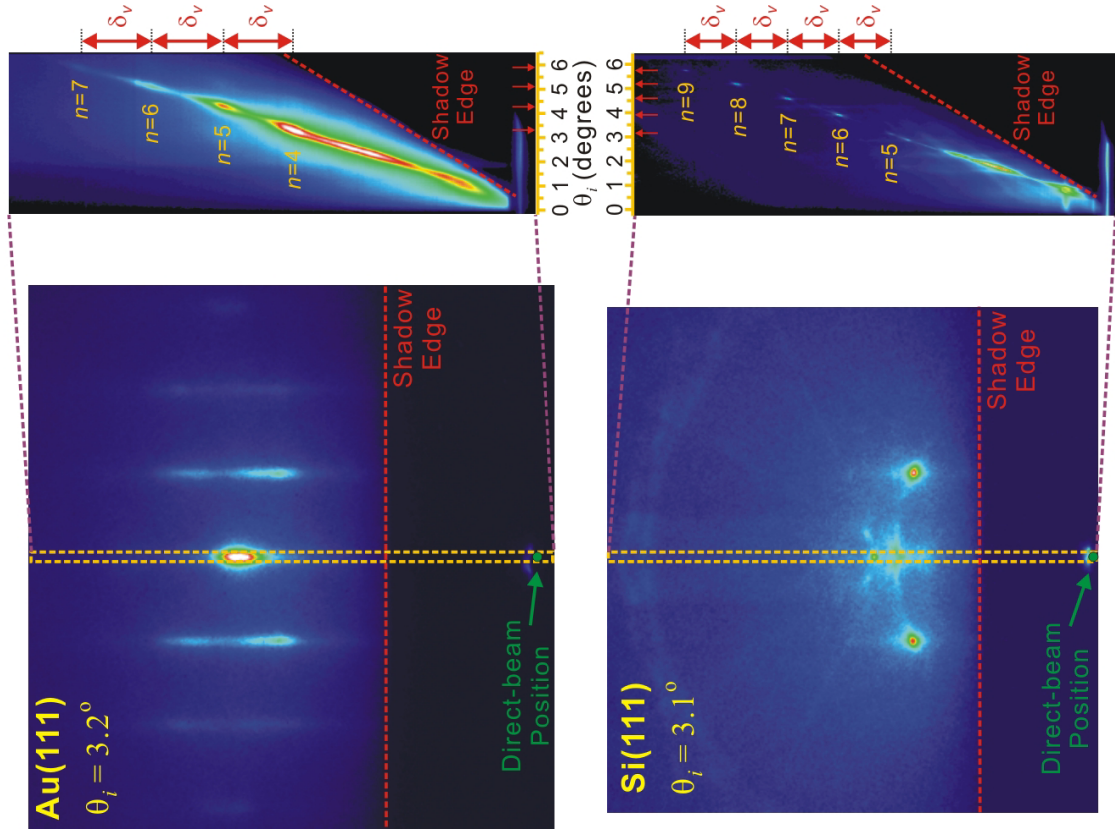


Fig. 8. Observed rocking curves for the (111) surface of gold and silicon. Rocking curves are obtained by recording diffraction patterns at different incidence angles. As the incidence angle is gradually increased, according to Ewald construction, Bragg spots will appear in-phase and out-of-phase alternatively. A narrow vertical strip along a streak is averaged horizontally for each image, resulting in a 1D intensity curve for each incidence angle. These curves are then combined into a 3D figure, i.e., intensity being plotted as a function of the incidence angle and vertical pixel number (a measure of s). At large incidence angles, the Bragg spots appear with regularity and, from both the vertical spacing (δ_v) and the change of incidence angle ($\Delta\theta$) between two consecutive diffraction orders, the interplanar distance d can be obtained. The indicated shadow edge is the outgoing electron scattering parallel to the surface.

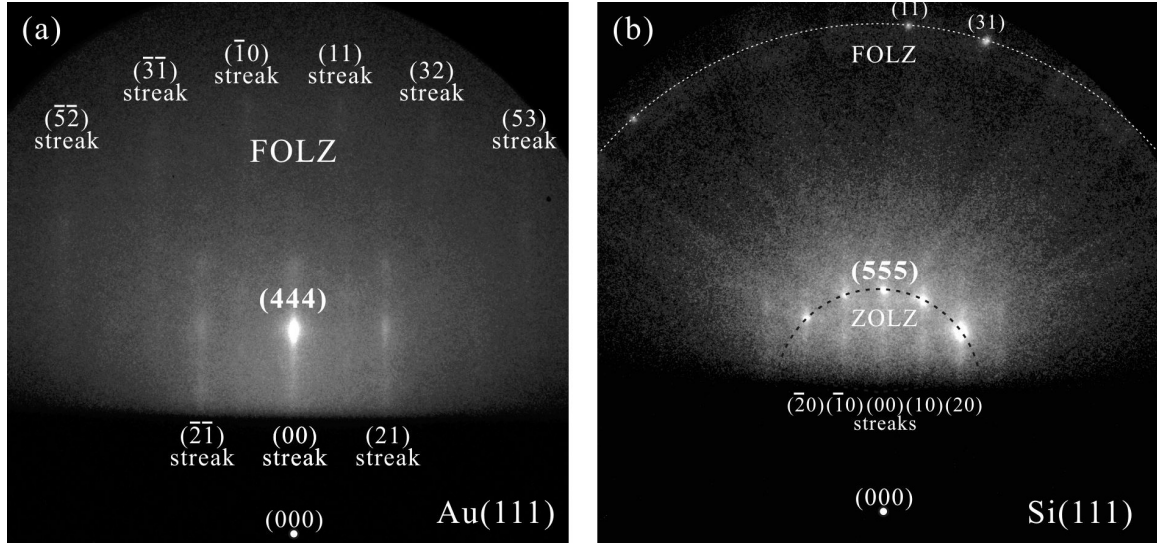


Fig. 9. Indexed diffraction patterns of (a) Au(111) and (b) Si(111). Indices for higher-order Bragg diffractions on the central streak are determined by using the Bragg condition (Eq. 21). Indices for streaks are assigned according to the 2D lattice of the surface plane. Diffractions from the first-order Laue zone (FOLZ) may be out of the camera region if the electron incidence angle is large.

that of silicon is illustrated in Fig. 8. Clearly, high-order Bragg spots appear with regularity, and we obtained $d_{\text{Au}(111)} = 2.36 \text{ \AA}$ and $d_{\text{Si}(111)} = 3.15 \text{ \AA}$ by using Eq. 21. These values are consistent with the x-ray literature values of the crystals.

Therefore, given the geometry of probing in RHEED, the central streak in the diffraction pattern contains the information about the interplanar distance along the surface normal; the evolution of the horizontal spacing between streaks with the azimuthal angle defines the symmetry of the 2D lattice in the surface plane, and gives the corresponding lattice constants. Although the RHEED technique is not intended for solving unknown crystal structures, it is designed to be used for the structural analysis of exposed crystal surfaces. In Fig. 9, two indexed patterns are shown as examples.

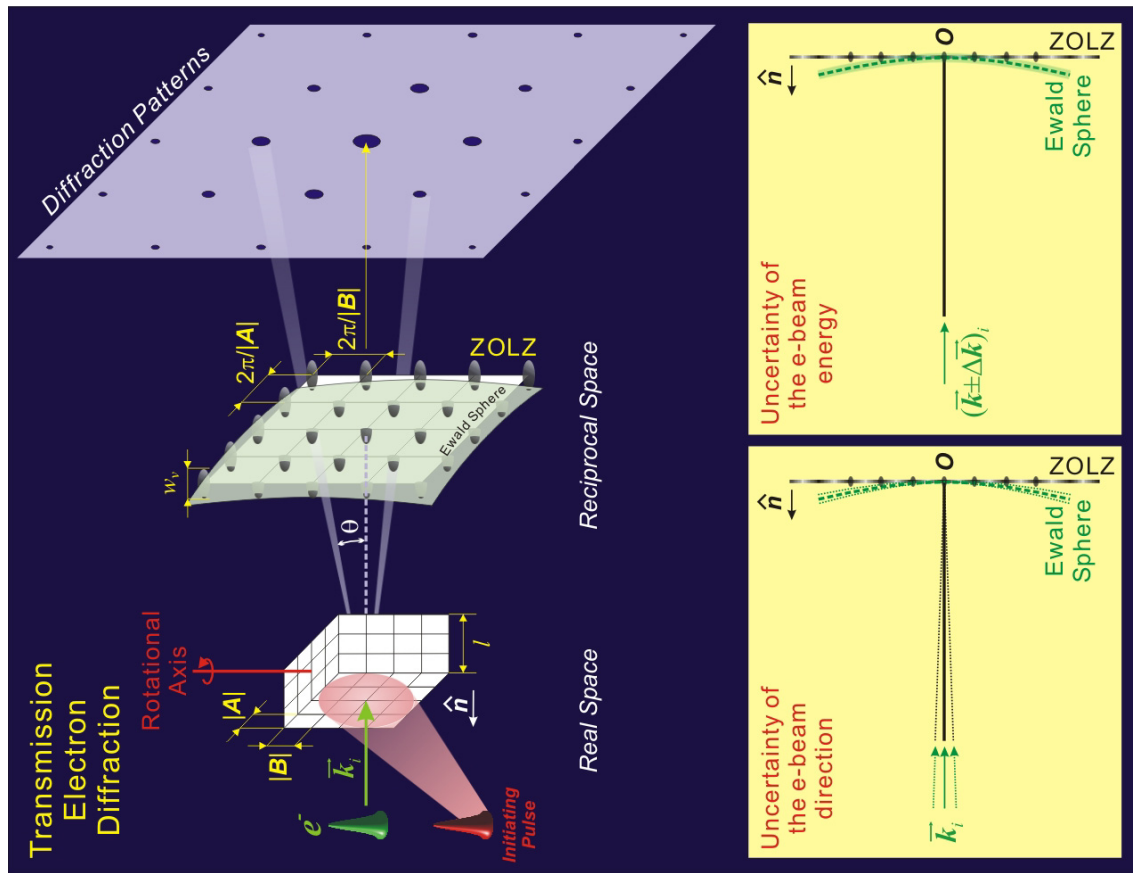


Fig. 10. Diffraction in transmission. Upper: Illustration of UEC methodology in this geometry. The finite thickness of a crystalline film results in the elongation of reciprocal-lattice points into rods along the surface normal \hat{n} . Consequently, the Ewald sphere can intersect with many rods and a pattern of Bragg spots of different orders will be formed. Lower left: The effect on Ewald construction due to the uncertainty in the direction of electron-beam propagation.

Such directional spread of the electron beam, which causes the Ewald sphere to wobble around the average axis, exists because of the Coulomb repulsion between electrons, i.e., spatial divergence which is reduced using the electron-gun focusing system. Lower right: The effect on Ewald construction due to the uncertainty in the electrons' kinetic energy. The Ewald sphere is given an additional thickness to allow for more intersections with the reciprocal lattice.

For a polycrystalline sample, namely, a sample consisting of many small crystallites randomly oriented in space, a diffraction pattern will show the Debye–Scherrer rings instead of spots. It is because the effective reciprocal lattice becomes a series of concentric spheres centered at the reciprocal space origin (a consequence of the random orientation in real space) and their intersections with the Ewald sphere give rise to rings. From the radial average, a 1D diffraction curve can be obtained; care must be taken and a fitting procedure is often necessary for the determination of the center, because a large part of the rings below the shadow edge is blocked. The peak positions correspond to the values of the reciprocal lattice vectors (\vec{G}_{hkl}) for different planes indexed by the Miller indices, (hkl) . The structure of the crystallites can be obtained by comparing the experimental data with the simulated diffraction curves for different crystal structures, as has been demonstrated in the UEC study of interfacial water (9).

A.3. Diffraction in Transmission

In contrast to the reflection mode, the diffraction patterns of crystalline thin films in transmission show many spots of different planes and orders. This is because of several reasons. First, due to the 2D-like thickness of the film in the \hat{n} direction, reciprocal lattice points are elongated into rods along \hat{n} , as mentioned previously. Figure 10 illustrates an example in which the electrons are propagating parallel to \hat{n} . According to Ewald construction, the origin of the reciprocal space (000) is on the Ewald sphere, and the ZOLZ plane is tangent to the sphere. If the reciprocal lattice consists of points only, no other spots [except the (000)] on the ZOLZ will be in contact with the sphere due to the sphere's curvature. However, because the reciprocal points are elongated (finite 2D thickness), the tips of the rods may intersect with the Ewald sphere so that more Bragg

spots appear in the diffraction pattern.

Second, when a macroscopic area is probed, the slight uncertainty of the crystal orientation across the thin film due to its unevenness will introduce a small angular span in the reciprocal lattice so that it has more chance to intersect with the Ewald sphere. Third, the finite spatial convergence/divergence of the electron beam provides an uncertainty of the direction of \vec{k}_i , which results in a solid cone around the average axis. Therefore, Ewald construction indicates that the sphere wobbles around that principal axis and sweeps a larger region in k space, allowing for more intersections (Fig. 10, lower left). Finally, the kinetic energy span of electrons, which causes the uncertainty of $|\vec{k}_i|$, gives the Ewald sphere an additional thickness to occupy a larger volume in k space. Hence, its intersection with reciprocal rods becomes more likely (Fig. 10, lower right).

Due to the aforementioned reasons, one can see that, in order to record more intense non-center Bragg spots, the crystalline film needs to be slightly rotated away from the original zone axis in order to optimize the overlap between the reciprocal rods and Ewald sphere. However, too much rotation can move the rods entirely away and result in no intersection. The span of rods in reciprocal space can be estimated from the rocking curves acquired through rotation of the crystalline film (along the vertical direction in Fig. 10) to change the incidence angle of the probing electrons, similar to the measurement of rocking curves in reflection experiments. The vertical width of rods (w_v) can be obtained from knowledge of the intensity angular profile of spots ($\Delta\theta_{hkl}$) because

$$w_v \approx G_{\perp} \Delta\theta_{hkl} \quad (22)$$

where G_{\perp} is the perpendicular component of G_{hkl} with respect to the rotational axis. We can also estimate the specimen thickness l over which diffraction is effective from the

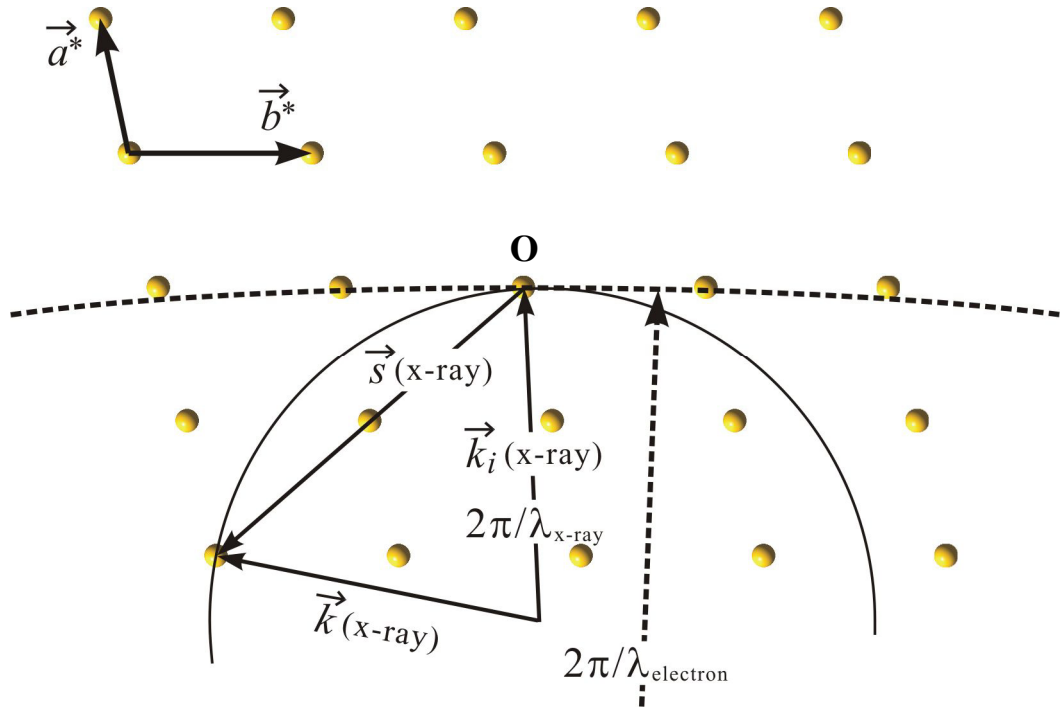


Fig. 11. Ewald construction in k space for electron and x-ray diffraction. The typical wavelength of high-energy electrons is much shorter than that of x-ray used for structure analysis, which leads to a much larger Ewald sphere for electrons (dashed arc) than that for x-ray (solid circle). The small-angle approximation can be used in the geometrical theory for electron crystallography and facilitate the visualization of the Laue condition.

Scherrer formula (7)

$$l \approx K\lambda / [\Delta\theta_{hkl} \cdot \cos(\theta/2)] = K \cdot 2\pi / w_v \quad (23)$$

where K (close to 1) is the shape factor of the average crystallite.

The structure of the 2D crystal is revealed in a single transmission diffraction pattern without rotation. From knowledge of the camera length and by Eq. 19, it is straightforward to obtain the lattice parameters. Of course, if the structure of the crystal under investigation is more complicated than that of a very thin, simple specimen consisting of light elements, one has to consider the issue of intensity, which may

additionally involve dynamical scatterings, but generally the determination of the orders of Bragg spots (lattice symmetry) can be obtained. As for a polycrystalline sample, similar procedures, as those discussed in the previous subsection, are used for structural determination.

A.4. Advantages and Selected Topics of Electron Diffraction

Throughout the previous description of the geometrical theory for electron diffraction, the small-angle approximation, $\sin\theta \sim \tan\theta \sim \theta$, was often made. As mentioned earlier, its validity comes from the order-of-magnitude difference between λ and d in Eq. 11. Furthermore, the corresponding Ewald sphere relative to the reciprocal lattice in k space has a large radius and, consequently, may be approximated as a plane. Therefore, visualization of the Laue condition through Ewald construction becomes a simpler task for high-energy electron diffraction, and fast calculations can be carried out to extract the lattice constants from recorded diffraction patterns. This also becomes an advantage for dynamics studies when correlating the observed diffraction changes as a function of time with actual transient modifications in the structures (which will be made clear from the discussion in the next section). In comparison, the typical wavelength of x-ray used for structure analysis is much longer, and the size of the corresponding Ewald sphere is, in fact, comparable to the reciprocal lattice vectors. It is easy to see from Fig. 11 that the Laue condition in Ewald construction for x-ray diffraction is less visual and involves more calculations than those presented above for electron diffraction. Reducing the x-ray wavelength is much more difficult compared to the case of electrons, which is readily attainable by increasing the acceleration voltage.

A.4.1 Surface Morphology and RHEED Pattern

The strong electron–matter interaction offers great opportunities for the studies of

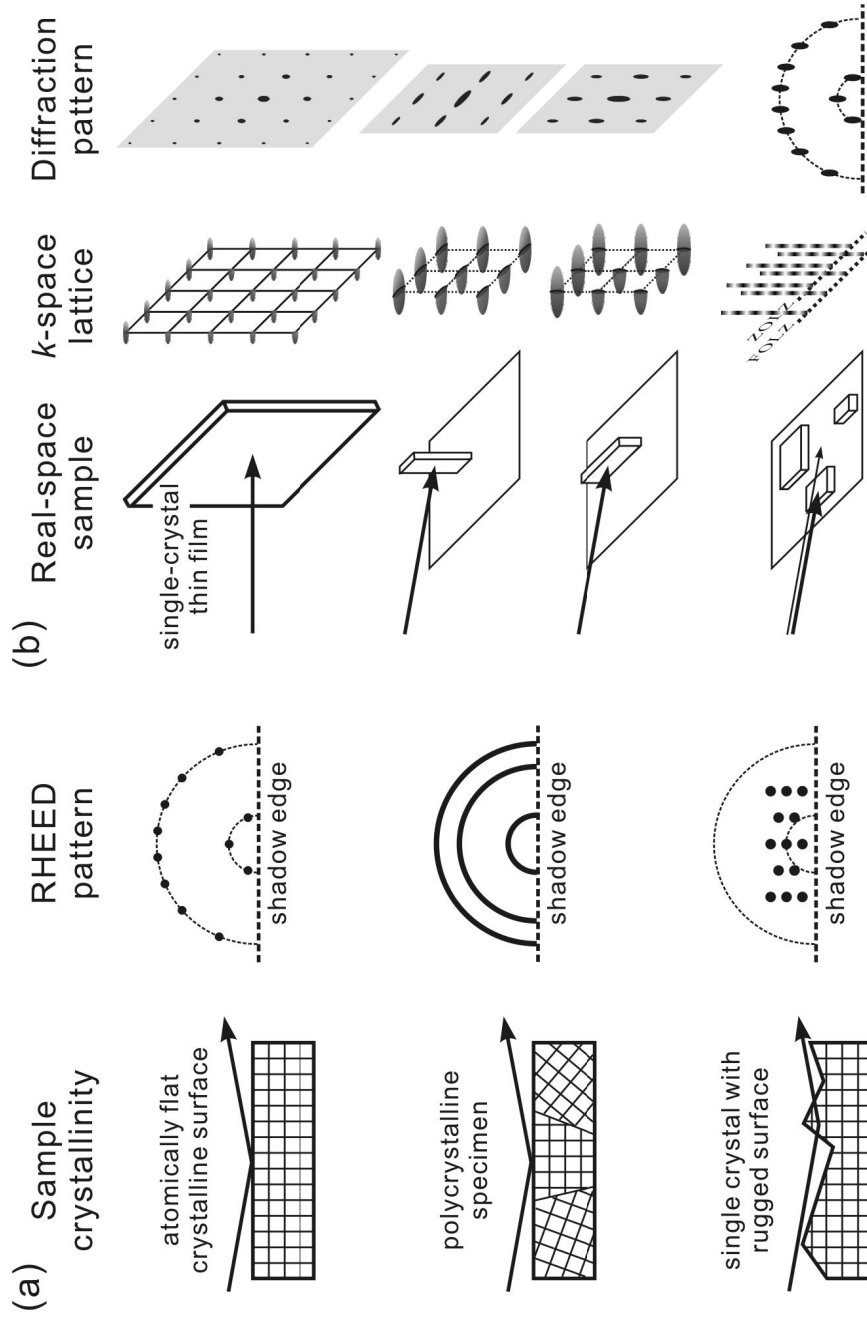


Fig. 12. Schematics for the correlation of (a) sample crystallinity and (b) surface morphology with the observed diffraction pattern. Sample conditions that produce ideal RHEED and transmission patterns are given in the upper panels. Even in reflection geometry, any type of electron penetration results in a transmission-like pattern (panel a, bottom, and panel b, middle). Increase of the spot width is along the direction of the crystallites' reduced dimension, a correlation dictated by the principle of Fourier transformation.

nanometer-scale structures and interfacial phenomena that are less straightforward for x-ray because of its large penetration depth and weak interaction with specimens in general. The same characteristic, however, also makes RHEED sensitive to the surface morphology of the specimen, whose studies in the fields of thin film growth and surface structure determination are actually the main application of this technique (6, 10, 11). From the types of diffraction patterns observed, the samples' crystallinity and surface morphology may be deduced, as illustrated in Fig. 12 (10). In principle, studies of structural dynamics can be made for all these cases as long as the diffraction spots or rings are distinct and well-defined; in practice, a sample surface that is close to atomically flat (at least within a certain 2D range) is more desirable because rough surface morphology often leads to decrease of diffraction intensity, increase of diffuse scattering background, and broadening of diffraction width that may hinder a proper analysis of temporal changes. Sometimes, well-oriented small crystallites that give a transmission-type pattern may be more beneficial to dynamics studies because of the cross reference obtained from different spots (see Chs. 6 and 7). The stringent requirement of atomically flat surfaces for studies is hence not always necessary.

A.4.2 Electron Mean Free Path and Penetration Depth

It is essential to estimate the electron penetration depth (ζ_e) at a given electron wavelength in a medium. This can be achieved by knowing the mean free path (ℓ_e) for elastic scattering from the total cross section of scattering (σ) and the density of scatterers (N), with the use of the following equations:

$$\ell_e = \frac{1}{\sigma N} \quad \text{and the differential cross section} \quad \frac{d\sigma}{d\Omega} = |f(\vec{s})|^2 \quad (24)$$

where Ω denotes the solid angle. With Eq. 5 and the angular integration of $d\sigma/d\Omega$, a screened-potential model that effectively describes the atomic potential for neutral

Table 1: Mean free paths and penetration depths for elastic scattering of electrons.

substance	Z	N (\AA^{-3})	ℓ_e (\AA) at 30 kV	ζ_e (\AA) at 30 kV
graphite	6	$2/(2.46^2 \cdot 6.70 \sin 60^\circ)$	2750	192 at $\theta_i = 4^\circ$
silicon	14	$8/5.43^3$	1010	70 at $\theta_i = 4^\circ$ 35 at $\theta_i = 2^\circ$
interfacial water (cubic form)	8 for O 1 for H	8/6.358 ³ for O 16/6.358 ³ for H	3050	53 at $\theta_i = 1^\circ$ (transmission-like)
gallium arsenide	31 for Ga 33 for As	$4/5.65^3$ for Ga and As	380	20 at $\theta_i = 3^\circ$
vanadium dioxide (monoclinic)	23 for V 8 for O	4/118 for V 8/118 for O	520	45 at $\theta_i = 5^\circ$
zinc oxide	30 for Zn 8 for O	$2/(3.25^2 \cdot 5.20 \sin 60^\circ)$ for Zn and O	370	20 at $\theta_i = 3^\circ$

elements in relation to the atomic number (Z) and a screening radius gives a good approximation for σ , especially when the scattering angle is not too small (11). The final result is

$$\sigma = 0.12 \lambda^2 Z^{4/3}. \quad (25)$$

The estimated mean free paths for elastic scattering and the corresponding penetration depths (at typical probing conditions) for several substances are given below in Table 1; their differences should be noted because, without the consideration of refraction,

$$\zeta_e \cong \ell_e \sin \theta_i \text{ (for single elastic scattering)}. \quad (26)$$

The simple estimation presented above shows that, with the criterion of energy- and momentum-conserved single scattering, electrons probe mostly the surface region of a specimen but do penetrate several unit cells (interplanar distances). The latter property is important in that UEC studies are still capable of resolving bulk-related structural dynamics, with a surface sensitivity. It should be noted that the values of penetration

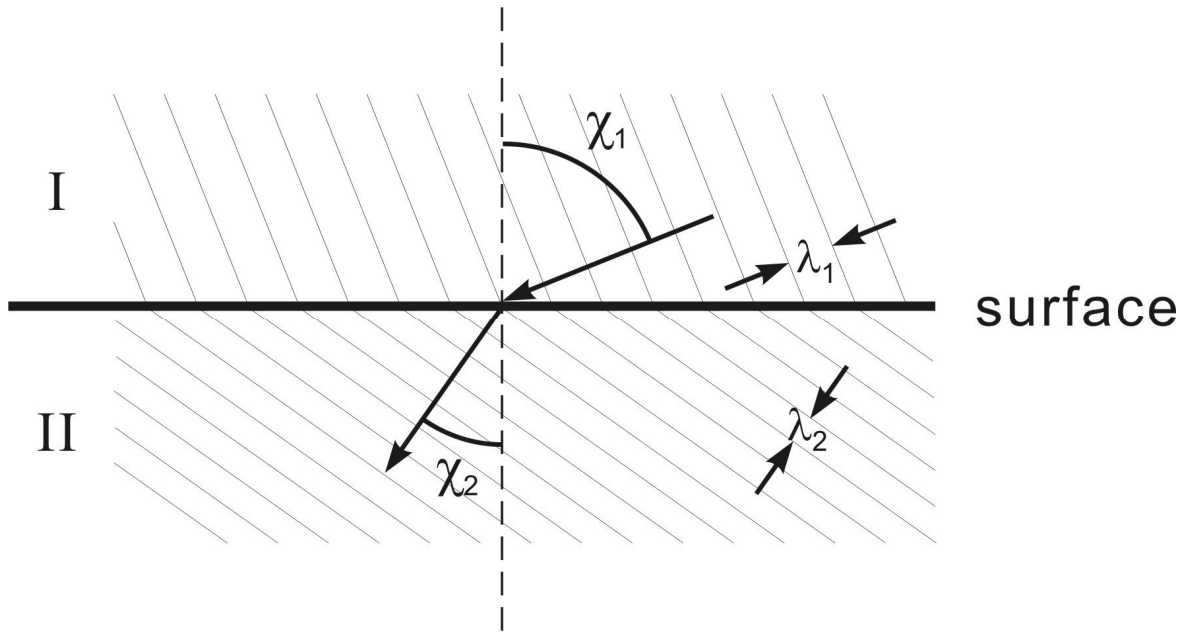


Fig. 13. Tangential continuity at the surface where the wave fronts are refracted. Medium II attracts electrons more than medium I, and the dashed line indicates the surface normal.

depth in Table 1 may be underestimated. If the surface morphology is less perfect than an atomically flat one, or more than one scattering event occurs so to contribute some diffraction intensities, electrons can reach a deeper region into the bulk. When a material contains much heavier elements (e.g., gold), the observed electron diffraction is expected to originate solely from the top layer and form streaks; an example can be seen in Fig. 5.

A.4.3 Inner Potential and Electron Refraction

The phenomenon of electron refraction occurs when the probing particles pass through the interface between vacuum and the specimen or between different materials. This phenomenon exists because electrons experience the difference of the electrostatic potential in different media. Compared to the vacuum environment, the superposition of the atomic potentials in a real material attracts and hence slightly accelerates an electron,

which leads to a small change in the wavevector. In an average sense without going into the structural details of atomic arrangement, the mean value of the crystal potential is called the inner potential, V_1 (in volts), typically a positive number for attraction. In Fig. 13, medium II has a higher V_1 than medium I, causing the traveling electrons to bend toward the surface normal.

Because the discontinuity of V_1 appears at the interface along the surface normal, the wavevector change should only occur in that direction. Thus, for a featureless interface, tangential continuity of the wave fronts is required, yielding an analogue of Snell's law in optics (11):

$$\frac{\sin \chi_1}{\lambda_1} = \frac{\sin \chi_2}{\lambda_2} \quad (27)$$

where χ_1 (χ_2) is the incident (refractive) angle with respect to the surface normal and λ_1 (λ_2) is the wavelength in medium I (II) (Fig. 13). With the use of Eq. 3, the relative refractivity can be written as

$$n_{12} = \frac{\sin \chi_1}{\sin \chi_2} = \sqrt{\frac{(V_0 + V_{12})[1 + 0.9785 \times 10^{-6} (V_0 + V_{12})]}{(V_0 + V_{11})[1 + 0.9785 \times 10^{-6} (V_0 + V_{11})]}} \cong 1 + \frac{V_{12} - V_{11}}{2V_0}. \quad (28)$$

The approximation is justified because the inner potentials V_{11} and V_{12} are generally much smaller than the acceleration voltage used. Furthermore, the small-angle approximation valid for typical RHEED experiments gives

$$\theta_i^2 = \left(\frac{\pi}{2} - \chi_1\right)^2 = \left(\frac{\pi}{2} - \chi_2\right)^2 - \frac{V_{12} - V_{11}}{V_0}. \quad (29)$$

As an example, for Si(111) with $V_1 \sim 11$ eV, the Bragg angles given by Eq. 11 (without taking into account the structure factor) are $\pi/2 - \chi_2 \approx n\lambda/2d_{\text{Si}(111)} = 11n$ mrad for 30-keV electrons; the corresponding θ_i 's for the first 8 orders are nonexistent, 11.4, 27.4, 40.2, 52.3, 64.0, 75.5, and 87.0 mrad, respectively. It is now clear why the regularity of Bragg

condition is restored for higher-order spots ($n \geq 5$) in the rocking curve shown in Fig. 8, lower right panel. The reflection of electrons by an atomically flat surface may be the major scattering events at very small incidence angles, which forms the specular spot that has little diffraction contribution for these probing conditions. As a result, UEC studies should be conducted with care with this phenomenon in mind.

A.4.4 Coherence of the Electron Beam

For electromagnetic waves, photons that are generated from a coherent source such as a monochromatic laser can propagate parallel and keep their phase because of their noninteracting nature; the plane-wave description by Eq. 1 is therefore appropriate. Such a model for the wave property of electrons has its limit in reality due to the following reasons. As mentioned earlier, any factor that causes the deviation of \vec{k}_i will lead to small changes in diffraction condition. Unlike photons, the Coulomb force causes electrons to interact with one another. As a result, collisions and the space-charge effect exist and destroy the coherence of charged particles, especially for a high-density beam. This issue may be reduced by lowering the number of electrons in a spatiotemporal bunch or totally eliminated by using single-electron packets (12).

However, real electron sources inevitably have finite sizes and energy spread that result in a finite angular spread ($\Delta\theta$) and the spread of the wavenumber (Δk). The effective coherence length (ξ) is a distance between two points from which the wave packet is scattered with a 180° phase difference (and hence no coherence) (11). From Δk and along the electron propagating direction,

$$\xi_{\parallel, \Delta k} = \frac{2\pi}{\Delta k} = \frac{\lambda^2}{\Delta\lambda} \cong \frac{24.52 \sqrt{V_0(1 + 0.9785 \times 10^{-6} V_0)}}{\Delta V (1 + 2 \times 0.9785 \times 10^{-6} V_0)} \quad (\text{in } \text{\AA}), \quad (30)$$

with the use of Eq. 3 and the assumption of the potential spread $\Delta V \ll V_0$. The value of

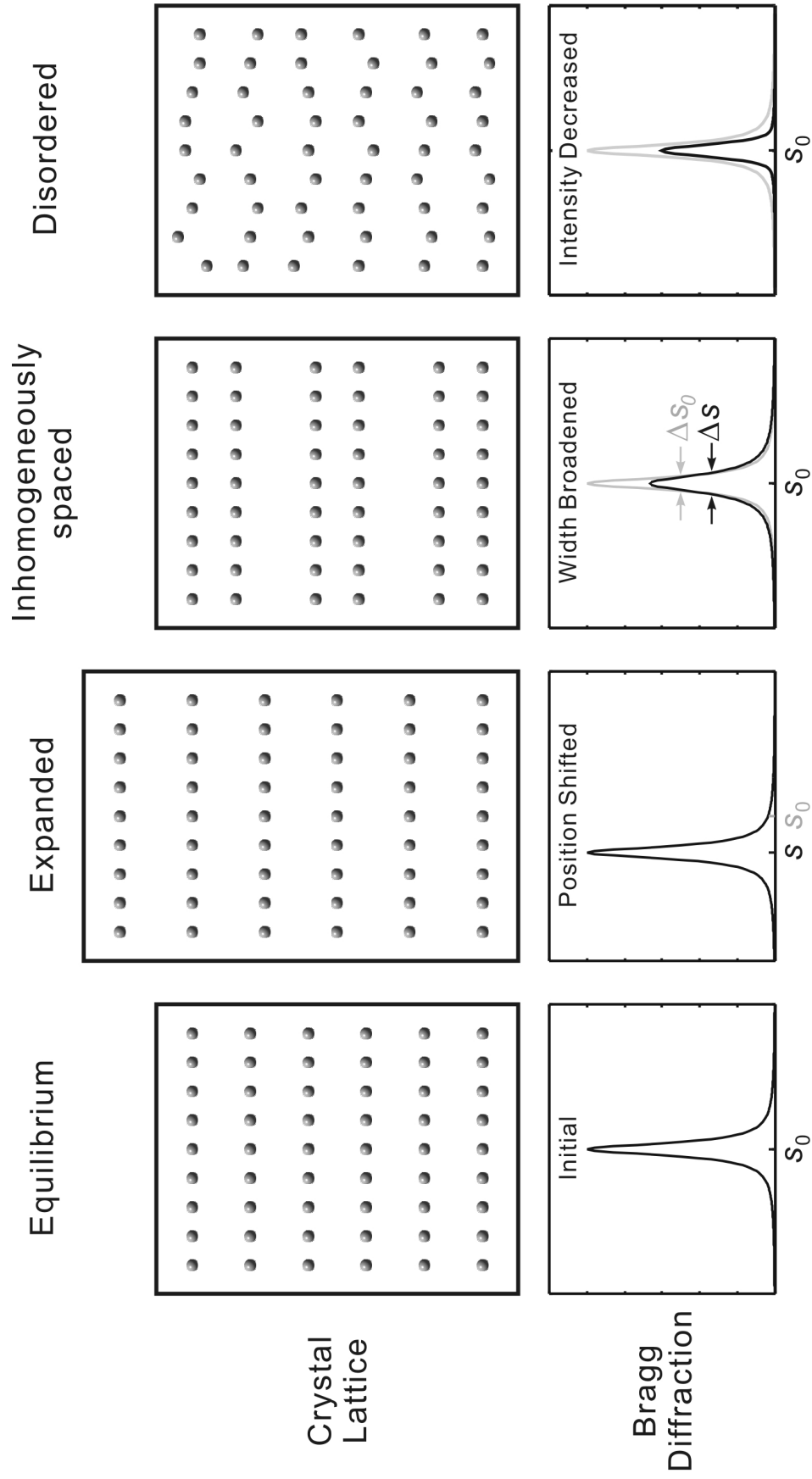


Fig. 14. Structural modifications in the crystal lattice and the corresponding diffraction changes. The diffraction differences observed as a function of time by UEC are therefore indicative of the different atomic motions in the lattice structure.

$\xi_{\parallel, \Delta k} \sim 41$ nm is obtained for $\Delta V = 10$ V and $V_0 = 30$ kV. From $\Delta\theta$ and perpendicular to the beam direction,

$$\xi_{\perp, \Delta\theta} = 2\pi/\Delta k_{\perp} = 2\pi/(k\Delta\theta) = \lambda/\Delta\theta \quad (31)$$

and has a value of about 7–70 nm for a typical $\Delta\theta$ of 1–0.1 mrad. The angular spread also results in a coherence length along the electron beam direction,

$$\xi_{\parallel, \Delta\theta} = \frac{2\pi}{\Delta k_{\parallel}} = \frac{\lambda}{\sin\theta_i \Delta\theta} \quad (32)$$

because $\Delta k_{\parallel} = \Delta(k \cos\theta) = k \sin\theta_i \Delta\theta$. For the aforementioned typical $\Delta\theta$ and at $\theta_i = 3^\circ$, $\xi_{\parallel, \Delta\theta}$ is about 130–1300 nm. The estimation of the coherence length above signifies that electrons generated by a real electron source can only “see” coherently a spatial range of the nanometer to sub-micrometer scale.

B. Nonequilibrium Transient Structures

In time-resolved experiments, the main diffraction features for studies of structural dynamics are the positions, intensities, widths, and the shapes of Bragg spots or Debye–Scherrer rings. Background intensity and Kikuchi patterns may also evolve as a function of time, but in general, their intensities and distributions are weak and diffuse. In the following discussion, we will focus on transient changes of the main diffraction features observed in UEC and make connections with x-ray studies (13–15). Summarizing in Fig. 14, in general, the position shift of Bragg spots or rings is directly related to lattice expansion or contraction; the change of the width and shape indicates the emergence of dynamical inhomogeneity; and the intensity change is the result of incoherent thermal motions, coherent lattice vibrations, or phase transitions.

B.1. Shifts of Diffraction Spots and Rings

Following an ultrafast excitation, diffraction spots or rings change their positions vertically and/or horizontally to reflect the changes in interplanar distances. Such changes

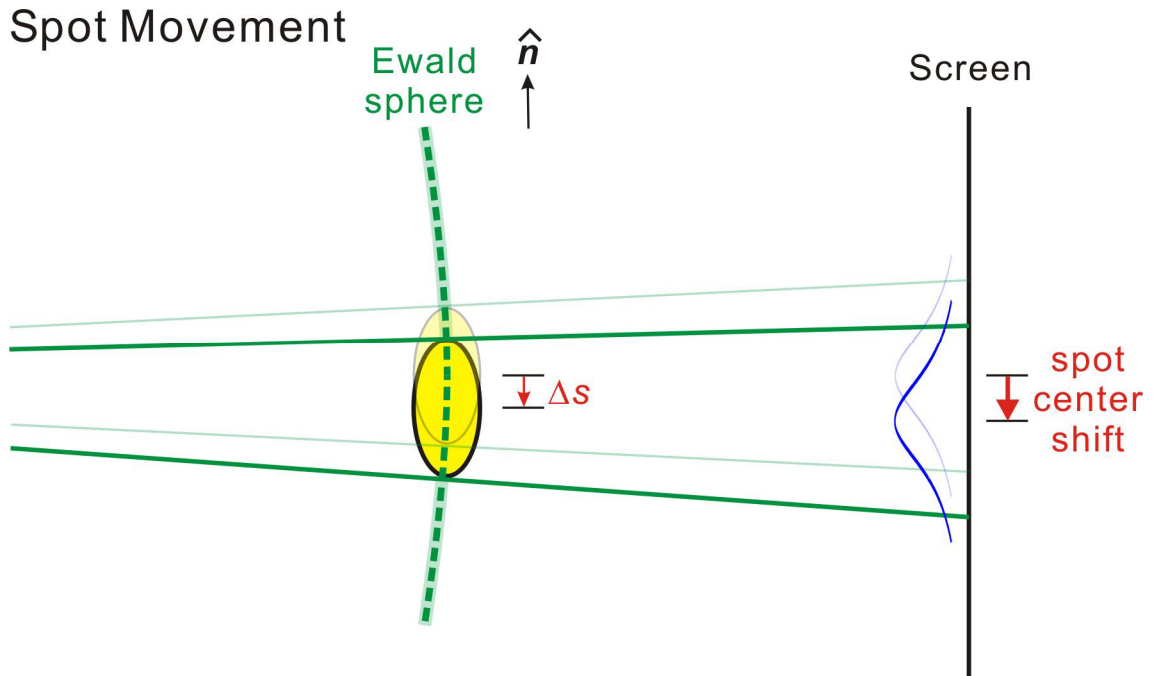


Fig. 15. Temporal changes of diffraction spot position. The faded rods and curves indicate the negative-time equilibrium configuration. As the real lattice expands along \hat{n} at positive times the reciprocal rods move downward, which leads to a downward movement of Bragg spots.

need to be homogeneous (uniformity of distance change) over essentially the entire spatially probed region, a requirement for preserving the Bragg condition. Thus, these shifts provide the unequivocal evidence for the homogeneous lattice expansion or contraction, depending on the direction of the shift.

We first consider the vertical lattice change along \hat{n} . According to the Laue condition of Eq. 12, a small vertical shift of the Bragg spot on the center (00) rod, $(0\mathbf{A}^* 0\mathbf{B}^*)$, is directly related to the change in the vertical lattice spacing by the following relationship:

$$\Delta s/s = -\Delta d/d = -\Delta(\theta/2)/\tan(\theta/2) \quad (33)$$

which becomes $-\Delta\theta/\theta$ when θ is small. Consequently, a decrease (increase) in s , i.e.,

when the Bragg spot shifts toward (away from) the direct beam position in the diffraction pattern, is a measure of the increase (decrease) in d . In reciprocal space, such a lattice change can be visualized as the rods moving parallel to \hat{n} and intersecting with the Ewald sphere but maintaining their size or shape (Fig. 15). The same picture can be applied to the description of movements in the horizontal direction.

On the ultrashort time scale, it is critical to understand the dynamics responsible for a downward shift, which is the observation made in many UEC studies. The first mechanism that comes to mind involves conventional heating, due to the anharmonicity of the lattice. The 1D thermal expansion is usually expressed as $\Delta x = (3g/4b^2)k_B\Delta T$, which is deduced from the anharmonic potential energy $U(x) = bx^2 - gx^3 - fx^4$ with positive b , g , and f (16). However, at room temperature, the (linear) thermal expansion coefficient (α_l) for most of the crystalline solids is on the order of 10^{-5} to 10^{-6} K^{-1} ; for example, $\alpha_l \times 10^6 = 2.6$, 5.73 and 14.2 for silicon, gallium arsenide and gold, respectively. Thus, a maximum *thermally driven* change of 1% in lattice spacing requires a lattice temperature jump of about 3850, 1750 and 700 K, which are not reachable at our excitation fluences and in a very short time. To achieve a temperature jump (ΔT_l) at the surface, the fluence for heating required is given by

$$F_{\text{heating}}/\delta = (F_{\text{laser}}/\delta)(1 - R)(E_{\text{excess}}/E_{\text{photon}}) \sim C_l\Delta T_l, \quad (34)$$

where δ is the penetration depth (inverse of the absorption coefficient, $1/\alpha$) of the light (photon energy E_{photon}) with fluence F_{laser} ; R is the reflectivity, E_{excess} is the above-gap excess energy, and C_l is the heat capacity of the lattice. For gallium arsenide, for example, $C_l = 1.74 \text{ J/cm}^3\text{K}$, the band gap $E_g = 1.423 \text{ eV}$, $R \sim 0.3$ (0.45) and $\delta \sim 710$ (6.4) nm for 800 (266) nm normal-incident light (17). A fluence of $F_{\text{laser}} = 10$ (1) mJ/cm^2 at 800 (266) nm gives the value of ΔT_l to be 4.6 K at 800 nm or 340 K at 266 nm.

Experimentally, this is in contradiction with the large observed shift. More importantly, as will be shown in Ch. 4, the spot-shifting behavior for the 800- and 266-nm excitations are contrary to the trend obtained above.

It follows that on the ultrashort time scale, the nonequilibrium state of the lattice must be considered. In this state, only certain types of the atomic motions may be initially launched, and the assumption of thermal equilibrium for all modes is not valid. Furthermore, carrier excitation can affect the lattice potential, resulting in a new state of weaker chemical bonding and hence a different structure. This expansion by a “*potential-driven*,” carrier-assisted mechanism does not depend on lattice temperature but on the carrier density. When the number of carriers decreases (through diffusion, for example), the expansion would decrease and the system recovers accordingly. Finally, the expansion in the vertical and horizontal directions may show anisotropy in the temporal behavior with different amplitudes for the change. Manifestation of these features of nonequilibrium behaviors can be seen in the studies made on GaAs (Ch. 4).

B.2. Changes of Widths and Shapes

The widths and shapes of Bragg spots or rings in a diffraction pattern are affected by the crystal size (Eq. 23), inhomogeneity and embedded strain in the sample, by electron refraction due to the shape of the crystallites (Sec. A.4.1), and by the uncertainty of the direction and magnitude of the probing electrons’ momentum $\hbar \vec{k}_i$ (size of the electron beam). However, their transient differences from a static reference can only stem from the structural changes induced by the optical excitation. In the case of polycrystalline samples, the average size of the crystallites may change (e.g., during ultrafast melting or annealing), resulting in the broadening or narrowing of diffraction rings according to the Scherrer formula (Eq. 23). The shape may also develop to a

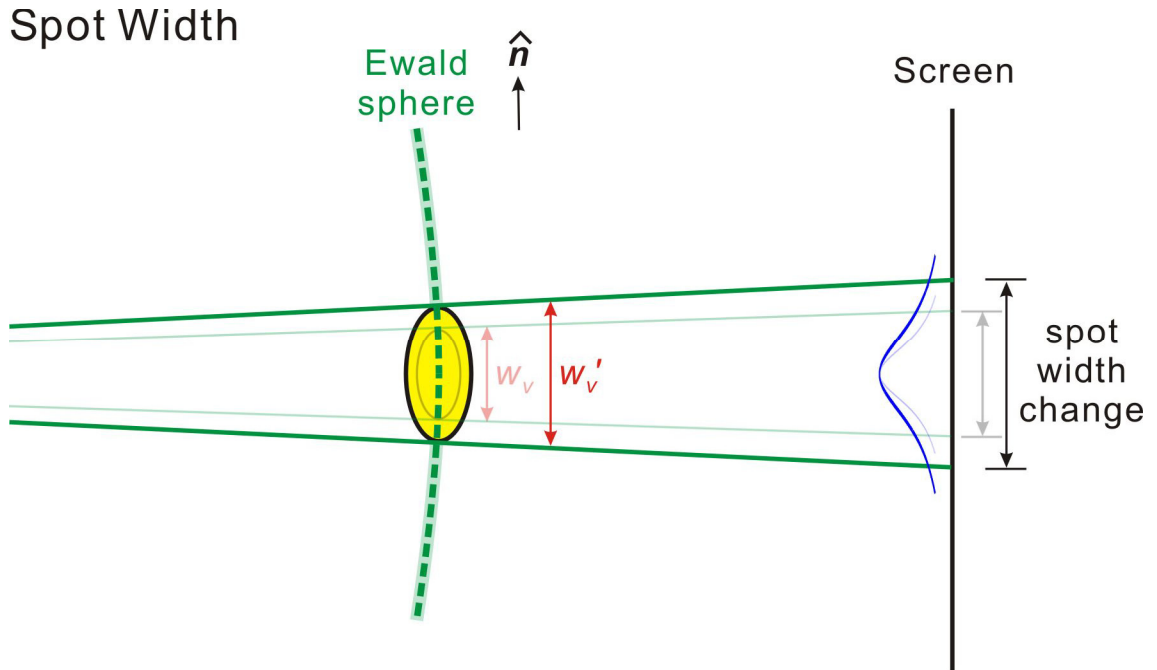


Fig. 16. Temporal changes of diffraction width. The faded rods and curves indicate the negative-time equilibrium configuration. Lattice inhomogeneity (along \hat{n}) generated in the crystal makes the reciprocal rods elongated, and their intersections with the Ewald sphere give a diffraction pattern with larger vertical width.

Gaussian-like function, which reflects an increased inhomogeneity. In the case of crystalline samples, however, this spatial size change is not of concern since the crystal essentially preserves its order. Thus, in this case, lattice inhomogeneity is due to a small modification of the average lattice spacing or a strain of propagating acoustic waves following the excitation.

Following the above discussion of the reciprocal-space picture, it is clear that, if the lattice planes evolve to two distributions of distances around d , one larger and one smaller, then this strain propagation will result in two side bands (or broadening) in k space around the central value (see Fig. 16). Such behavior is commonly caused by an acoustic sound wave of relatively small wavelength. Coherent acoustic motions are

typically generated through carrier excitation or from the decay of another type of initially generated lattice vibration, e.g., optical phonons. In an elementary metal, acoustic phonons are directly generated following carrier generation because only one atom exists in the primitive unit cell and there is no optical branch. However, in a semiconductor with more than one atom in the primitive unit cell, optical phonons are present and become the doorway for efficient coupling with the carriers. These optical phonons have a lifetime during which they convert to acoustic ones, and the latter into thermal motions on a time scale determined by the anharmonicity of the lattice.

The inhomogeneity of the lattice generated parallel to the sample surface, i.e., the horizontal broadening of reciprocal-lattice rods, has a more complicated effect: when intersecting with the Ewald sphere, the rod projects not only a larger horizontal width but also an enlarged vertical width in a diffraction pattern. However, the geometry of RHEED allows the contributions to horizontal and vertical widths due to the dynamical inhomogeneity of the lattice along different directions to be distinguished (see Appendix B for the derivation). By monitoring the temporal evolution of spot widths in the directions orthogonal to \hat{n} , lattice dynamics along the surface can be followed as a function of time. The difference between the temporal evolution along the vertical and horizontal directions in the diffraction patterns can provide information of such anisotropy. As will be shown in Ch. 4, a key cause of the anisotropy is free movement along the \hat{n} direction (surface vertical vs bulk lateral) and the change in lattice potential.

B.3. Changes of Diffraction Intensities

On the basis of Eq. 9, the diffraction intensity of a Bragg spot (hkl) is proportional to the square of the geometrical structure factor $F(hkl)$, which is given by (5)

$$F(hkl) = \sum_j f_j \exp(-i \vec{G}_{hkl} \cdot \vec{r}_j) = \sum_j f_j \exp[-2\pi i (h x_j + k y_j + l z_j)] \quad (35)$$

where f_j is the atomic scattering factor of the j th atom in a primitive unit cell. Since the determination of $F(hkl)$ involves the positions of atoms, $\vec{r}_j \equiv (x_j, y_j, z_j)$, in a unit cell, any lattice motions that appreciably change their relative positions can cause the diffraction intensity to change. These motions are those of optical phonons (see, e.g., Refs. 13–15 and 18), small-wavelength acoustic phonons, and the thermal motions. In contrast, homogeneous lattice expansion or contraction has no influence on the intensity of the Bragg spots. The contribution of the thermal, incoherent motion (in all directions) in diffraction intensities can be calculated using the DW expression, Eq. 16.

The ability in UEC to resolve the diffraction in time and for different Bragg spots makes possible the separation of contribution by these different processes, especially that horizontal and vertical lattice motions manifest themselves differently. The change of spot intensity on the (00) rod will display vertical motions, whereas those on the side will have contributions from both vertical and horizontal motions. However, incoherent thermal motion affects all of the Bragg spots. For the case of gallium arsenide as an example, this separation is clear. The crystal has a face-centered-cubic lattice with a two-atom basis that has gallium at $\vec{r}_{\text{Ga}} \equiv (0, 0, 0)$ and arsenide at $\vec{r}_{\text{As}} \equiv (1/4, 1/4, 1/4)$ in the unit cell in the equilibrium state. If, say, \hat{n} is [001], the intensity of the Bragg spot (0 0 4n) on the (00) rod is proportional to

$$|F(0\ 0\ 4n)|^2 = |f_{\text{Ga}} \exp(-8n\pi i z_{\text{Ga}}) + f_{\text{As}} \exp(-8n\pi i z_{\text{As}})|^2. \quad (36)$$

Thus, those optical phonons that have the Ga and As atoms vibrate against each other along the vertical direction (e.g., longitudinal optical phonons) will affect the structure factor and consequently the diffraction intensity. Horizontal vibrational motions, however,

have no influence because their projection on the vertical scattering vector is zero. On the other hand, if thermal motion is responsible for the intensity reduction, Equation 16 provides the theoretical description. By monitoring the extent and time scale of the intensity reduction for different Bragg spots, the lattice motions responsible for the observed changes can be distinguished.

B.4. Transient Changes in Transmission Diffraction

Because of the probing geometry in the transmission mode, transient diffraction patterns of crystalline thin films can directly provide the dynamic information in the 2D structure. Due to the intersection between rods and the Ewald sphere, as shown in Fig. 10, 2D lattice expansion/contraction deduced from decrease/increase of the distances between diffraction spots, or changes of structural homogeneity indicated by the width changes, can be observed experimentally. Transient structural information along the \hat{n} direction could be masked, given the experimental geometry where the electron beam propagation is essentially in the same direction of rods (see Sec. A.3 for discussion). Naturally, if there is substantial lattice expansion along \hat{n} on the picosecond time scale, such change can be observed in the reflection geometry. In transmission, however, this \hat{n} -direction lattice motion can lead to intensity changes, as will be shown in Ch. 4.

Transmission electron diffraction has also been applied to studies of polycrystalline metallic thin films by several groups, e.g., those of Miller (19), Cao (20), and, earlier, Mourou (21). The issues of nonthermal solid-to-liquid phase transition and electronically driven lattice changes have been discussed. However, due to the polycrystalline nature of the sample, transient lattice motions in a single crystallite and those between randomly oriented crystallites may be strongly correlated, and this could complicate the interpretation of structural dynamics. The transmission study reported in

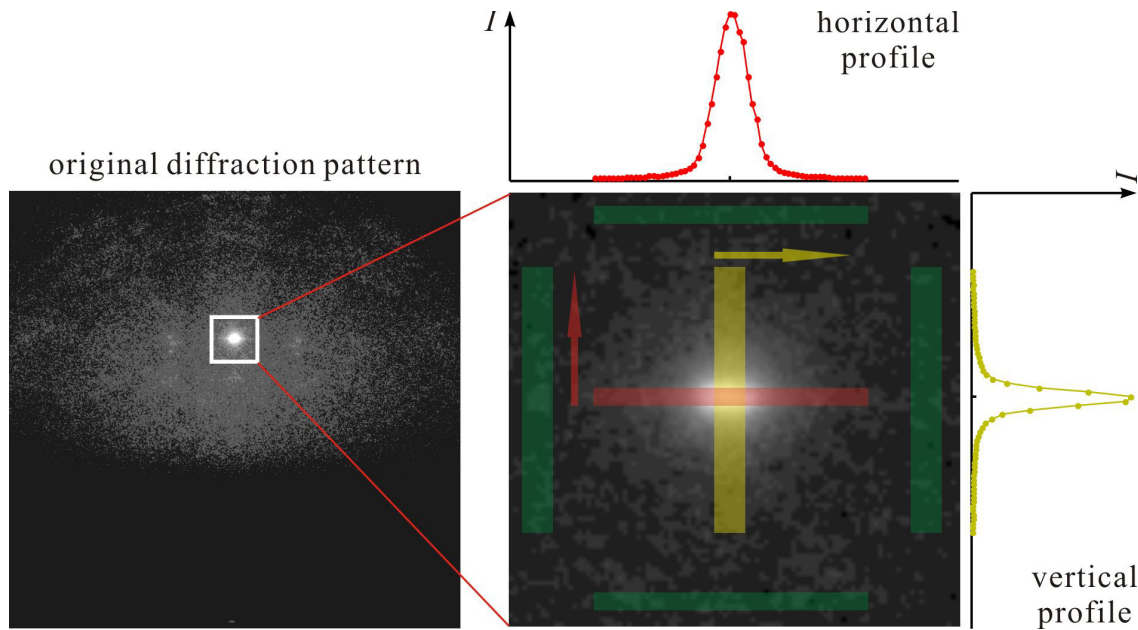


Fig. 17. Extraction of the horizontal and vertical profiles of a Bragg spot. The narrow strips (yellow for the vertical direction and red for the horizontal) are the regions over which intensity averaging is performed. Profiles obtained from the green strips (vicinity of the Bragg spot) may be used for background subtraction when necessary.

Ch. 4 was, to our knowledge, the first study of structural dynamics of a single-crystal semiconductor by electron diffraction, which displays the motion of the entire lattice.

B.5. Extraction of Transient Diffraction Changes

To quantify the aforementioned diffraction changes at transient times, a fitting procedure is invoked to obtain the intensity, position, width and line shape of a Bragg spot or diffraction ring as a function of time. For typical UEC studies, the analysis can be made in 1D by considering the vertical and horizontal directions separately. The first step is to collect the 1D profiles of a certain diffraction feature at different times, by averaging over a narrow strip across the diffraction vertically or horizontally (Fig. 17). The important issue here is to achieve a higher ratio of the signal to the background and noise. The profile obtained from a wider strip may be less noisy but with a lower peak due to

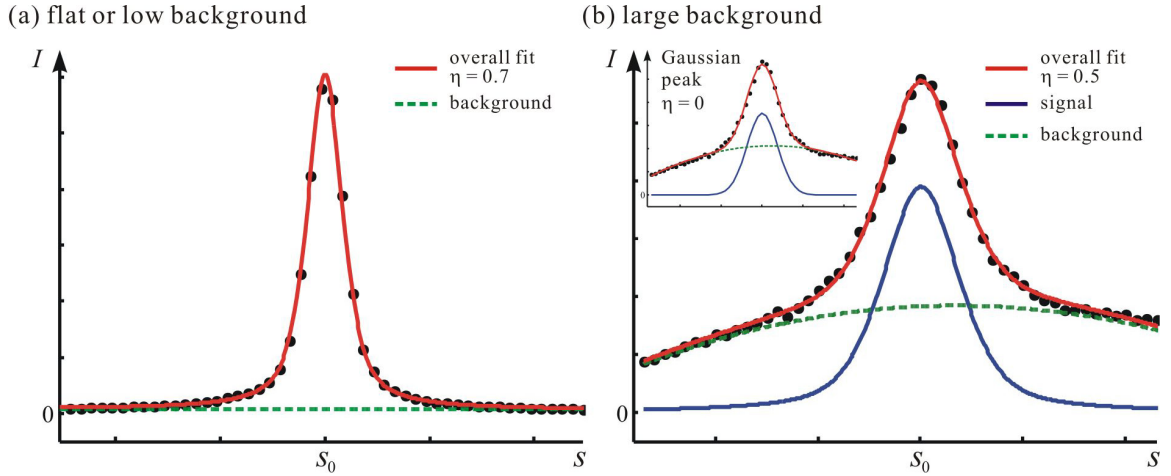


Fig. 18. Results of the fit. (a) A constant offset or linear function is included in the fit of an intensity profile with a flat or low background. (b) A quadratic (or higher-order) function is used for the background. The inset shows the result of the fit that considers a pure Gaussian form for the signal; the small discrepancy is visible.

the background in the less intense part; the profile from a narrower strip contains more contribution from the signal, but can be less smooth. Thus, a balanced choice may be a strip that covers (approximately) the horizontal or vertical full width at half maximum.

For fitting, a pseudo-Voigt shape function, $f_{pV}(s)$, is used,

$$f_{pV}(s) = I \cdot [\eta \cdot f_L(s) + (1 - \eta) \cdot f_G(s)], \quad (37)$$

$$f_L(s) = \frac{1}{\pi} \cdot \frac{w/2}{(s - s_0)^2 + (w/2)^2},$$

$$f_G(s) = \frac{2}{w} \sqrt{\frac{2 \ln 2}{\pi}} \exp\left(\left(\frac{s - s_0}{w}\right)^2 \cdot 4 \ln 2\right).$$

The integral of $f_L(s)$ or $f_G(s)$ over s is unity (normalized), and Eq. 37 is a simple sum of the two functions instead of a convolution (Voigt shape). Here, I represents the (1D) integrated intensity, s the scattering vector coordinate, s_0 the peak position, w the (common) full width at half maximum, and η the Lorentzian contribution. Depending on the surface quality and the electron incidence angle, the diffuse background may be low

and flat enough such that no subtraction prior to fitting is needed (Figs. 17 and 18a); when the background is not negligible, either a subtraction by the profile obtained from the vicinity of the diffraction feature is made first, or a polynomial (typically quadratic) function is include in the fit (Fig. 18b).

Comparisons between the extracted diffraction features— $I(t)$, $s(t)$, $w(t)$, and $\eta(t)$, where t is the delay time between the electron and optical pulses—are subsequently made to elucidate the structural dynamics and relaxation pathway in the specimen. Based on the previous discussion in Secs. B.1 to B.3, the similarity or difference between these time-dependent features can provide crucial information about the involvement of the candidate (structure-related) physical processes, their synchrony or sequence in time, and the characteristic time constants that govern the structural dynamics.

B.6. Issues of Electron Refraction and Scalability of Diffraction Change

Two issues about the dynamical changes in UEC are addressed. The first one is in regard to the diffraction changes caused by the electron refraction effect. According to the discussion in Sec. A.4.3, the two reasons are the possible slight tilting of the surface normal and the change of the inner potential, both of which result from the optical excitation and may lead to small change in the diffracted beam direction. However, it can be shown from the order-of-magnitude analysis that electron refraction plays a minor role in the diffraction changes discussed above, for typical UEC studies with moderate optical excitation.

The tilting of \hat{n} comes from the different extent of lattice expansion as a result of the gradient of the excitation pulse profile on the specimen. This effect may be much reduced by using a sample size or making the probed area within the region of relatively homogeneous excitation. Furthermore, with the total vertical expansion of the lattice on

the order of 1 to 10 Å over the length of the probed region along \vec{k}_i (on the order of 1 mm), electron refraction may cause an angular change of 10^{-4} to 10^{-3} mrad, much less than the uncertainty of \vec{k}_i itself and consequently unimportant. The inner potential of matters is on the order of 10 V, and its change induced by moderate excitation is expected to be on the order of 1 V or less. Thus, from Eq. 29, the induced angular shift would be on the order of $10^{-3.5}$ mrad and hence negligible. For intense excitation, the electron refraction effect due to larger surface or bulk potential change may be observed (22); however, care has to be taken in interpreting the relative shifts of diffraction features, which is the next issue discussed below.

On the basis of Eq. 33, diffractions from the same set of crystal planes with different orders (n) are expected to exhibit shifts in proportion to n during the structural dynamics, with the same (normalized) temporal evolution for the movements. In addition, the accompanying changes in their intensities, if exist, should be scalable according to Eq. 16 or Eq. 35, and follow one temporal profile only. The presumption behind is that all of these diffractions originate from spatially the same part of the probed specimen. However, if, for some reason, this is not the case, the scalability of diffraction shifts may not hold; an additional observation that often accompanies with this somewhat counterintuitive phenomenon will be the different time constants for diffractions of different orders.

It should be noted that a pattern of many spots similar to the cases shown in Fig. 12, bottom of panel a and upper three of panel b, comes with a transmission nature. Due to the different electron traveling directions for different diffractions, lower-order spots may originate spatially from the higher part of a crystallite (to avoid the blocking of diffracted electrons by adjacent crystallites or surface structures) and the highest-order

one is formed by diffracted electrons that penetrate deeper. The key governing factor here is the mean free path discussed in Sec. A.4.2. Such a phenomenon will be further discussed in Ch. 5 with a real case. Proportionality of diffraction shifts becomes true for solely transmission-type experiments such as studies of polycrystalline samples (electrons penetrating small crystallites and forming the diffractions), and an example can be seen in Ch. 10. For scalability of intensity changes, see Ch. 4 for the transmission case and Ch. 8 for the reflection case.

Appendix A. Conventions

In the diffraction theory, the incoming beam is described by Eq. 1. In this convention, the wavenumber $k = |\vec{k}_i| = 2\pi/\lambda$, and for electrons, $k = \omega/v$ where $v = \lambda\nu$ is the velocity and $\nu = \omega/2\pi$ is the frequency; the momentum of the particle $p = \hbar k = m\nu$, and the de Broglie relation $\lambda = h/p$ which consistently equals to $2\pi/k$. Accordingly, when k is used in this form, a constant factor of 2π appears in diffraction expressions of k , s and others such as the reciprocal basis vectors in 3D (Eqs. 13 and 14), those for a 2D reciprocal lattice (Eq. 16), and the last part of Eq. 23.

Crystallographers use a different convention to define the wavevector, $k = \lambda^{-1}$. As such the factor 2π disappears, and, for example, the important relations $\vec{s} \cdot \vec{R} = 2m\pi$ and $s = (4\pi/\lambda)\sin(\theta/2)$ become simply $\vec{s} \cdot \vec{R} = m$ and $s = (2/\lambda)\sin(\theta/2)$. In such a way, it is straightforward to invert s directly into real-space distances. The crystallography convention is equivalent to rewriting Eq. 1 for $\Psi_0(\vec{r}', t)$ with the phase factor being $2\pi\vec{k}_i \cdot \vec{r}' - \omega t$, where the new k_i is $1/\lambda$. The important point is to keep track of the self-consistency regarding the momentum as the conventional $p = \hbar k$, or $p = hk$ with k

being clearly defined. Unfortunately, these definitions, with or without 2π , are used in different areas of diffraction. For example, in gas-phase diffraction, s is defined with 2π included; for most of the following chapters, this convention is used.

Similarly, the definition of the angle of incidence being θ or $\theta/2$ requires a convention. Considering θ to be the total diffraction angle (see Fig. 2a), the incidence angle would be $\theta/2$; if the incidence angle is θ , then the total scattering angle would be 2θ . The definition of s follows.

Appendix B. Reciprocal-space Broadening of Rods

The following simple estimation is made for the effect of horizontal broadening of the rods in reciprocal space on the observed width of diffraction spots. For an ordered structure in 2D, the reciprocal lattice is made of rods, and when modulated by the spacings in the \hat{n} direction, each zone should be considered as a symmetric-top-like shape with $w_h = w_x, w_y$ being different from $w_v = w_z$. Therefore,

$$(2x/w_h)^2 + (2y/w_h)^2 + (2z/w_v)^2 = 1$$

where x and y are the directions (in reciprocal space) orthogonal to \hat{n} , z the direction parallel to \hat{n} , and w_h (w_v) is the full horizontal (vertical) width. Locally, the Ewald sphere with large radius (large $\hbar k_i$) will cut through the rods nearly as a tilted plane (Fig. 16) defined by $(0, 1, 0)$ and $(\sin\gamma, 0, \cos\gamma)$, where γ is the angle between \hat{n} [i.e., $(0, 0, 1)$] and plane direction. As a result, the elliptical trace where the rod and the plane intersect has a horizontal width w_h but the vertical width becomes $(\tan^2\gamma/w_h^2 + 1/w_v^2)^{-1/2}$.

If, due to horizontal inhomogeneity, w_h becomes $w_h + \Delta w_h$, the change of the vertical width will be

$$\Delta w_h \tan^2\gamma / [\tan^2\gamma + (w_h/w_v)^2]^{3/2},$$

which is much less than or on the same order of Δw_h . This is because in the reflection geometry of UEC, γ is small and w_v and w_h are not significantly different within an order of magnitude. It is noted that w_v and w_h are determined by the inverse of the coherence length (on the order of 10 nm or more) and also affected by the specimen morphology.

References:

1. B. K. Vainšhtein, *Structure analysis by electron diffraction* (Pergamon Press, Oxford, 1964).
2. H. M. Seip, in *Selected topics in structure chemistry*, P. Andersen, O. Bastiansen, S. Furberg, Eds. (Universitetsforlaget, Oslo, 1967), pp. 25-68.
3. J. C. Williamson, Ph.D. thesis, California Institute of Technology (1998).
4. Z. L. Wang, *Elastic and inelastic scattering in electron diffraction and imaging* (Plenum Press, New York, 1995).
5. N. W. Ashcroft, N. D. Mermin, *Solid state physics* (Saunders College Publishing, Fort Worth, TX, 1976), pp. 101-108.
6. Z. L. Wang, *Reflection electron microscopy and spectroscopy for surface science* (Cambridge Univ. Press, Cambridge, 1996).
7. B. E. Warren, *X-ray diffraction* (Dover, New York, 1990), pp. 38, 253.
8. J. F. Vetelino, S. P. Gaur, S. S. Mitra, *Phys. Rev. B* **5**, 2360 (1972).
9. C.-Y. Ruan, V. A. Lobastov, F. Vigliotti, S. Y. Chen, A. H. Zewail, *Science* **304**, 80 (2004).
10. P. K. Larsen, P. J. Dobson, Eds., *Reflection high-energy electron diffraction and reflection electron imaging of surfaces* (Plenum Press, New York, 1988).
11. A. Ichimiya, P. I. Cohen, *Reflection high-energy electron diffraction* (Cambridge

- Univ. Press, Cambridge, 2004).
12. A. Gahlmann, S. T. Park, A. H. Zewail, *Phys. Chem. Chem. Phys.* **10**, 2894 (2008).
 13. A. Rousse, C. Rischel, J.-C. Gauthier, *Rev. Mod. Phys.* **73**, 17 (2001).
 14. C. Bressler, M. Chergui, *Chem. Rev.* **104**, 1781 (2004).
 15. M. Bargheer, N. Zhavoronkov, M. Woerner, T. Elsaesser, *Chemphyschem* **7**, 783 (2006).
 16. C. Kittel, *Introduction to solid state physics* (John Wiley & Sons, Inc., New York, 7th ed., 1996), pp. 129-131.
 17. S. Adachi, *Optical constants of crystalline and amorphous semiconductors: Numerical data and graphical information* (Kluwer Academic Publishers, Boston, 1999), pp. 221, 225.
 18. K. Sokolowski-Tinten *et al.*, *Nature* **422**, 287 (2003).
 19. B. J. Siwick, J. R. Dwyer, R. E. Jordan, R. J. D. Miller, *Chem. Phys.* **299**, 285 (2004).
 20. S. H. Nie, X. Wang, H. Park, R. Clinite, J. M. Cao, *Phys. Rev. Lett.* **96**, 025901 (2006).
 21. S. Williamson, G. Mourou, J. C. M. Li, *Phys. Rev. Lett.* **52**, 2364 (1984).
 22. R. K. Raman *et al.*, *Phys. Rev. Lett.* **101**, 077401 (2008).